

ELECTRICAL CHARACTERIZATION
OF
6H CRYSTALLINE SILICON CARBIDE

STEPHEN E. LEMPNER
Bachelor of Electrical Engineering
Cleveland State University
August, 1988

Submitted in partial fulfillment of the requirements
for the degree
MASTER OF SCIENCE IN ELECTRICAL ENGINEERING
at the
CLEVELAND STATE UNIVERSITY
August, 1994

This dissertation has been approved for the Department of
Electrical Engineering and the College of Graduate Studies

Mangju Ghalla Goradia Sept 9, '94
Dr. Mangju Ghalla-Goradia

Lawrence G. Matus Sept 9, 1994
Dr. Lawrence G. Matus

Chandra Goradia Sept. 9, 1994
Dr. Chandra Goradia

James A. Lock Sept 9, 1994
Dr. James A. Lock

Edward J. Haugland 9/9/94
Dr. Edward J. Haugland

J. Anthony Powell Sept. 9, 1994
Mr. J. Anthony Powell

ACKNOWLEDGEMENTS

This research was sponsored by and conducted at the Instrumentation and Control Technology Division of the NASA Lewis Research Center in Cleveland, Ohio. It was also sponsored in part by the College of Graduate Studies of the Cleveland State University.

I thank my thesis advisor, Dr. Manju Ghalla Goradia, who has been an inspiration to me, and through whose efforts the opportunity to conduct this research was provided. Not only has she been an advisor but a friend as well. She has reviewed and edited this work and protected me from the burdens of paperwork that accompanies research.

I thank Dr. Lawrence Matus, my project sponsor at NASA, who encouraged me to develop my own ideas and provided helpful advice. I thank Mr. J. Anthony Powell for providing informative and thoughtful comments. I thank Dr. Edward Haugland for the many insightful discussions on theoretical and experimental matters and on data analysis, and for graciously taking the time to analyze the data with his double level model.

I am also grateful to Mr. J. Anthony Powell, Mr. Carl Salupo, and Mr. Robert Allen for their help in providing and preparing the samples for this experiment and to Dr. Chandra Goradia, Dr. James Lock, Dr. Edward Haugland and Mr. J. Anthony Powell for reviewing this thesis.

I especially thank Dr. Chandra Goradia for his guidance and help during the final stages of preparation of this thesis.

I thank Mrs. Janet Basch for typing part of this thesis and making corrections during its initial stage of writing.

Most of all I want to thank my Mom, Mildred Riley, for her love and support. She instilled in me her love of learning, and her sense of humor has come to the rescue on numerous occasions.

I also want to thank my sister, Dorothy Schadl, for our talks, on a universe of topics. Her candor has been both refreshing and necessary.

ELECTRICAL CHARACTERIZATION OF
6H CRYSTALLINE SILICON CARBIDE

STEPHEN E. LEMPNER

ABSTRACT

Crystalline silicon carbide (SiC) substrates and epilayers, undoped as well as n- and p-doped, have been electrically characterized by performing Hall effect and resistivity measurements (van der Pauw) over the temperature range of approximately 85 K to 650 K (200 K to 500 K for p-type sample). By fitting the measured temperature dependent carrier concentration data to the single activation energy theoretical model: 1) the activation energy for the nitrogen donor ranged from 0.078 eV to 0.101 eV for a doping concentration range of 10^{17} cm⁻³ to 10^{18} cm⁻³, 2) the activation energy for the aluminum acceptor was 0.252 eV for a doping concentration of 4.6×10^{18} cm⁻³. By fitting the measured temperature dependent carrier concentration data to the double activation energy level theoretical model for the nitrogen donor: 1) the activation energy for the hexagonal site was 0.056 eV and 0.093 eV corresponding to doping concentrations of 3.33×10^{17} cm⁻³ and 1.6×10^{18} cm⁻³, 2) the activation energy for the cubic site was 0.113 and 0.126 eV corresponding to doping concentrations of 4.2×10^{17} cm⁻³ and 5.4×10^{18} cm⁻³.

TABLE OF CONTENTS

	Page
ABSTRACT	v
LIST OF TABLES	x
LIST OF FIGURES	xi
LIST OF SYMBOLS	xiv
CHAPTER	
I. INTRODUCTION	16
II. THEORY	5
2.1 Hall Effect	5
2.2 van der Pauw Method	10
2.3 Measurements	11
2.4 Activation Energy from Carrier Concentration	13
2.4.1 Single Level Model	13
2.4.2 Double Level Model	15
2.5 Activation Energy from $n(T)$ and $\rho(T)$ at low Temperatures.	17
2.6 Measurement Accuracy	19
2.6.1 Error Due to Contact Size	19
2.6.2 Calculation of Error in the Final Result	19
2.7 Extraneous Effects	22

CHAPTER	Page
III. SAMPLE PREPARATION	28
3.1 Growth of 6H-SiC Epilayers	28
3.2 Contacts	29
3.3 Mask	31
IV. APPARATUS	38
4.1 Hall Setup	38
4.2 Cryostat and Sample Jig	39
4.3 Temperature Measurement & Control	40
4.4 Electrical Measurement	41
V. Results and Discussion	43
5.1 Review of Past Work	43
5.1.1 Single Activation Energy Impurity Level System	45
5.1.2 Double Activation Energy Impurity Level System	45
5.2 Results and Discussion	47
5.2.1 Single Activation Energy Level Analysis	50
5.2.2 Results of Activation Energy From Low Temperature $n(T)$ and $\rho(T)$	56
5.2.3 Double Activation Energy Level Analysis	56
5.2.4 Results of $\mu_H(T)$	60
5.3 Summary	61

CHAPTER	Page
5.4 Recommendations for Future Work . . .	62
BIBLIOGRAPHY	63
APPENDICES	67
A. Tables	67
B. History and Nomenclature of SiC	69
B.1 Introduction	69
B.2 History	70
B.3 Structure and Nomenclature	74
C. Least Squares	77
C.1 Introduction	77
C.2 Least Squares Method	77
C.3 Least Squares Applied	79
D. Cryostat Schematics	86
E. Effective Mass	91

LIST OF TABLES

Table		Page
I.	Calculated Thermo-(electric and magnetic) Effects	27
II.	Current and Resistivity Values for $\Delta T = 0.5$ K from Equations (52) and (53) . .	36
III.	Highest Resistivity Encountered	37
IV.	Two Level Activation Energies	48
V.	Room Temperature ρ , μ_H and carrier concentration for the test samples.	49
VI.	Calculated Activation Energy and Impurity Concentrations from the Single Level Model.	51
VII.	Calculated Activation Energy and Impurity Concentrations from the Double Level Model.	59
VIII.	Parameter Values (Si, Ge, GaAs, 6H-SiC) . .	67
IX.	Calculated Figures of Merit at 300 K . . .	68
X.	Polytype Notation	76

LIST OF FIGURES

Figure	Page
1. Charge Carriers in a Magnetic Field	6
2. Arbitrarily Shaped Flat Sample	10
3. Resistivity Configurations	12
4. Carrier concentration as a function of temperature for the undoped Cree substrate B04365-5B with error bars.	23
5. Carrier concentration as a function of temperature for the undoped Cree substrate B0428-2H with error bars.	23
6. Carrier concentration as a function of temperature for the undoped NASA grown epilayer 1312-3 with error bars.	24
7. Carrier concentration as a function of temperature for the aluminum doped NASA grown epilayer 1270-2 with error bars.	24
8. Epilayers	29
9. Mesa Mask Layout	31
10. RIE Pin-wheel Pattern	32
11. Dimensioned Hall Bar	34
12. Dimensioned van der Pauw Pattern	35
13. Sample Platform and Probe	40
14. van der Pauw Connections	41

Figure	Page
15. Energy Levels	46
16. Carrier concentration as a function of temperature for the undoped Cree substrate B0436-5B.	52
17. Resistivity as a function of temperature for the undoped Cree substrate B0436-5B.	52
18. Carrier concentration as a function of temperature for the undoped Cree substrate B0428-2H.	53
19. Resistivity as a function of temperature for the undoped Cree substrate B0428-2H.	53
20. Carrier concentration as a function of temperature for the undoped NASA grown epilayer 1312-3.	54
21. Resistivity as a function of temperature for the undoped NASA grown epilayer 1312-3.	54
22. Carrier concentration as a function of temperature for the aluminum doped NASA grown epilayer 1270-2.	55
23. Resistivity as a function of temperature for the aluminum doped NASA grown epilayer 1270-2.	55
24. Carrier Concentration as a function of temperature (double level model, sample B0436-5B).	58

Figure	Page
25. Carrier Concentration as a function of temperature (double level model, sample B0428-2H).	58
26. Carrier Concentration as a function of temperature (double level model, sample 1312-3).	59
27. Mobility as a function of temperature for the four test samples.	61
28. Acheson Furnace	70
29. Lely Chamber	72
30. Modified Lely Chamber	73
31. Close Packed Spheres	75
32. High temperature furnace and sample holder. . .	86
33. Firebrick machining dimensions.	87
34. The machined firebrick and magnet's pole piece.	88
35. Bottom of the sample platform.	89
36. Top of the sample platform and thermocouple support.	90

LIST OF SYMBOLS

B	Magnetic flux density.
E_a	Acceptor activation energy.
E_{ac}	Cubic site acceptor activation energy.
E_{ah}	Hexagonal site acceptor activation energy.
E_B	Electric breakdown field.
E_c	Conduction band edge.
E_d	Donor activation energy.
E_{donor}	Donor energy level.
E_{dc}	Cubic site donor activation energy.
E_{dh}	Hexagonal site donor activation energy.
E_F	Fermi energy level.
E_H	Hall electric field intensity.
E_o	Optical-phonon energy.
F_m	Lorentz force.
H	Magnetic field intensity.
I	Current.
J	Current density.
J_q	Heat current.
k	Boltzmann constant.
m^*	Effective mass (electrons or holes).
m_d^*	Density of states effective mass (electrons or holes).
m_{de}^*	Density of states effective mass of electrons.

m_{dh}^*	Density of states effective mass of holes.
m_o	Electron rest mass.
n	Charge carriers per unit volume.
N_a	Total acceptor concentration per unit volume.
N_a^-	Ionized acceptor concentration per unit volume.
N_c	Impurity concentration per unit volume for cubic sites.
N_{comp}	Compensating impurity concentration per unit volume.
$N_{c,v}$	Effective density of states in the conduction or valence band.
N_d	Total donor concentration per unit volume.
N_h	Impurity concentration per unit volume of hexagonal sites.
R_H	Hall coefficient.
r_H	Hall factor.
s_x	Calculated standard deviation of x .
ΔT	Temperature difference.
ΔT_E	Ettingshausen temperature difference.
ΔT_S	Righi-Leduc temperature difference.
$t_{\alpha,\phi}$	Student's t -distribution parameter.
V_E	Ettingshausen voltage.
V_{ES}	Ettingshausen-Seebeck voltage.
v_d	Drift velocity of charge carriers.
V_H	Hall voltage.
v_L	Saturated drift velocity.

V_N	Nernst voltage.
V_{RH}	Variance of the Hall coefficient.
V_S	Seebeck effect voltage.
V_t	Variance of the sample thickness.
V_{VH}	Variance of the Hall voltage.
Z_J	Johnson figure of merit.
Z_K	Keyes figure of merit.
α_o	Thermoelectric coefficient.
B	Spin degeneracy factor.
ϵ	Static dielectric constant.
ϵ_d	Reduced activation energy.
η	Reduced Fermi energy.
κ	Thermal conductivity.
κ_e	Electronic thermal conductivity.
μ	Drift mobility.
μ_H	Hall mobility.
π_1	Peltier coefficient of material in which current is entering.
π_2	Peltier coefficient of material from which current is leaving.
ρ	Resistivity.
$\Delta\rho$	Error in resistivity measurement.

CHAPTER 1

INTRODUCTION

The interest in silicon carbide (SiC) stems from properties that make it suitable for applications difficult or impossible for other semiconductors to duplicate. It is an adamantine refractory material with a wide bandgap. Further, it is chemically inert and radiation tolerant [1], making it suitable for use in extreme environments. Other outstanding properties of SiC include its high breakdown field E_b , a high saturated drift velocity v_L (v_L is the velocity at which the electron has enough energy to emit an optical phonon [2], $v_L = \sqrt{(8E_o)/(3\pi m^*)}$ [3], where E_o is the optical-phonon energy and m^* is the effective mass of the electron), and a high thermal conductivity κ (at room temperature and below, silicon carbide has a higher thermal conductivity than that of pure copper; at room temperature the thermal conductivity of 6H-SiC is 4.9 W/cm K as compared to 4 W/cm K for copper [4]).

SiC crystallizes in several forms. This research is restricted to the form known as 6H-SiC. Table 8 in Appendix

A gives some of the parameter values for 6H-SiC at room temperature, along with those of Si, Ge and GaAs for comparison¹.

Several figures of merit have been developed to compare how the physical and electrical properties of semiconductors would affect their device performance. Two widely used figures of merit [5,6] combine the saturated drift velocity with the breakdown field or thermal conductivity to determine frequency and power limitations of the material.

The Johnson (1965) figure of merit, Z_J , uses the breakdown field and the saturated drift velocity to arrive at a measure of the high frequency and high power capability of devices. It is written as

$$Z_J = \frac{E_B^2 * V_L^2}{4 * \pi} \quad (\text{V/sec})^2 \quad (1)$$

where Z_J sets an upper limit on the combination of device parameters, namely, the maximum power output P_m , the maximum operating frequency F_m , and the maximum load impedance Z_m [2,5].

The Keyes (1972) figure of merit, Z_K , emphasizes the thermal conductivity limitations of devices. It is written

¹ Appendix B gives a brief history of silicon carbide and its nomenclature.

$$Z_K = \kappa \left(\frac{c * V_L}{4 * \pi * \epsilon} \right)^{\frac{1}{2}} \quad (\text{W/sec-}^\circ\text{C}) \quad (2)$$

Here, c is the speed of light and ϵ is the static dielectric constant of the material. Z_K includes small size effects. Smaller devices have higher speed, limited by the saturated drift velocity, and higher device density increases power dissipation per unit area [2].

The figures of merit illustrate that the properties of SiC lend themselves to power, microwave, and elevated temperature applications; not, however, to small devices operating at room temperature [2], because of the large bandgap which would cause, for a given doping concentration, the width of the depletion region to be higher in SiC devices than in devices made of lower bandgap materials. This in turn would limit the theoretical size reduction possible.²

The purpose of this research was to electrically characterize bulk and epilayer 6H-SiC samples. The electrical characterization consisted of Hall voltage and resistivity measurements so as to determine the majority carrier concentrations and mobilities. The values of majority carrier concentration over a wide range of temperature allow determination of the dopant concentration

² Table 9 in Appendix A gives calculated values of Johnson's and Keyes' figures of merit for Si, Ge, GaAs and 6H-SiC.

and its activation energy. Such a characterization is a necessary first step in both basic materials research and in the development and understanding of useful devices.

CHAPTER 2

THEORY

This chapter presents the theory of how the carrier concentration and mobility values are derived from Hall voltage and resistivity measurements. Also presented is the theory of how the dopant concentration and its activation energy are obtained from the temperature dependence of the majority carrier concentration. This is followed by the theory of measurement accuracy and possible extraneous effects.

2.1 Hall Effect

E. H. Hall devised an experiment in 1879 [45,46] to determine the nature of the force acting on a material carrying a current in a magnetic field. He found that by setting a magnetic field \mathbf{H} perpendicular to a strip of the material through which current I is flowing, a force develops perpendicular to both the current and magnetic field. This force is $\mathbf{F}_m = I\mathbf{l} \times \mathbf{B}$, where \mathbf{l} is the directed

length of the strip along the direction of current flow, and B is magnetic flux density. This force is due to the combined effect of the Lorentz force $q\mathbf{v}_d \times \mathbf{B}$ acting on each charge carrier within the conductor. Here \mathbf{v}_d is the drift velocity of charge carriers and q is the magnitude and sign of the charge on the carriers. As seen in Figure 1, for the same direction of conventional current and the magnetic

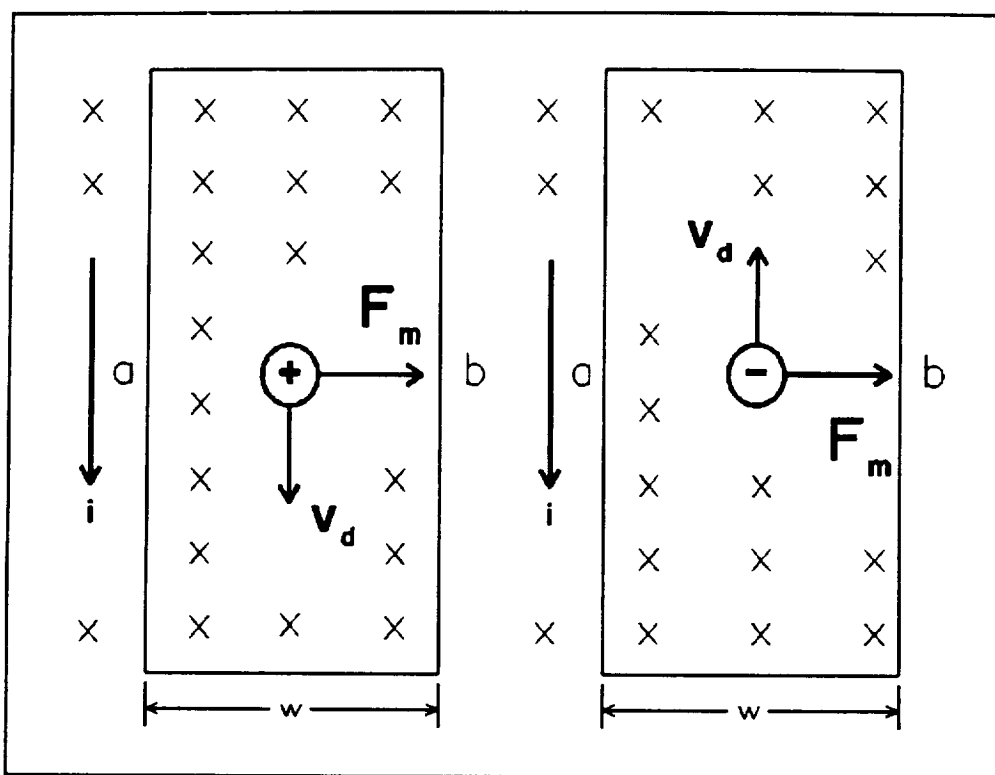


Figure 1 Charge Carriers in a Magnetic Field

field, the direction of the Lorentz force is the same on both electrons and holes. This produces a transverse Hall potential

$$V_H = \int_a^b \mathbf{E}_H \cdot d\mathbf{w} = \mathbf{E}_H w \quad (3)$$

between the sides of the strip, where w is the width of the test strip and E_H is the Hall electric field intensity. The sign of this potential determines the sign of the majority charge carriers.

The Hall electric field E_H builds to the point where it just cancels the force caused by the magnetic field.

$$qE_H = q(\mathbf{v}_d \times \mathbf{B}) \quad (4)$$

For an n-type extrinsic sample, the number of charge carriers per unit volume, n , can be found from Hall effect measurements. Since \mathbf{v}_d and \mathbf{B} are perpendicular to each other, $E_H = v_d B$ and since

$$v_d = \frac{J}{n q} \quad (\text{cm/sec}) \quad (5)$$

where J is the current density in the strip, the carrier concentration is given by

$$n = \frac{J B}{q E_H} \quad (6)$$

or, in terms of measurable quantities

$$n = \frac{I B}{q t V_H} \quad (\text{cm}^{-3}) \quad (7)$$

where t is the thickness of the test strip along the direction of the magnetic field.

The Hall coefficient R_H is defined as the ratio of the Hall electric field to the product of current density and magnetic flux density [44]. It is written

$$R_H = \frac{E_H}{J B} \quad (8)$$

or, in terms of measurable quantities

$$R_H = \frac{V_H t}{I B} \quad (\text{cm}^3/\text{C}) \quad (9)$$

Comparing Eq.(7) and Eq.(9), the Hall coefficient $R_H = 1/nq$. However, R_H is commonly expressed as

$$R_H = \frac{r_H}{n q} \quad (10)$$

where the meaning of the Hall factor r_H will become clear shortly.

The signs of the Hall coefficient and the Hall voltage are the same; if conduction is due to electrons they are negative, if it is due to holes they are positive.

Drift mobility is defined as the ratio of the drift velocity v_d to the electric field intensity E parallel to the current flow, and is written

$$\mu = \frac{v_d}{E} \quad (\text{cm}^2/\text{V sec}) \quad (11)$$

Resistivity ρ is defined as the ratio of the electric field intensity, parallel to the current flowing in the material, to the current density.

$$\rho = \frac{E}{J} \quad (12)$$

Substituting for the current density J from Eq. (5) we get

$$\rho = \frac{E}{n q v_d} \quad (13)$$

Using Eq. (10) and Eq. (11) gives

$$\rho = \frac{|R_H|}{r_H \mu} \quad (\Omega \text{ cm}) \quad (14)$$

for the resistivity of the material.

The Hall mobility μ_H is defined as

$$\mu_H = \frac{|R_H|}{\rho} \quad (\text{cm}^2/\text{V sec}) \quad (15)$$

Combining Eqs. (14) and (15) we get the relationship between Hall mobility and drift mobility, $\mu_H = r_H \mu$, where r_H is the Hall factor which is usually close to one and is a function of the energy-dependent relaxation time which is dependent on the scattering mechanism(s) involved [49].

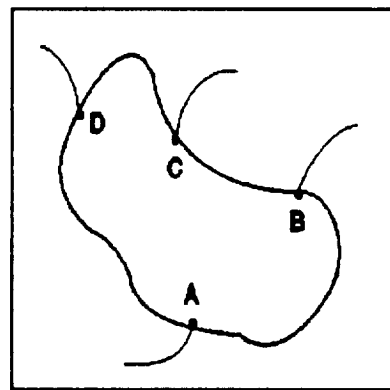
2.2 van der Pauw Method

In 1958, L. J. van der Pauw published a theorem [42] for measuring the specific resistivity and Hall coefficient of flat lamella of arbitrary shape. This can be done without knowing the current pattern in the sample if the following conditions are met.

1. The contacts are at the periphery of the sample.
2. The contacts are of negligibly small area.
3. The sample has uniform thickness and has no holes.

The four needed contacts can be placed in an arbitrary way along the periphery of the sample, as shown in Fig. 2.

The resistivity is calculated from two resistance measurements R_1 and R_2 as defined below. When a current I_1 is passed into A and out of B, measuring V_1 the potential difference between V_D and V_C ($V_1 = V_D - V_C$), gives resistance $R_1 = V_1/I_1$. In a similar way resistance $R_2 = V_2/I_2$ is found by



F i g u r e 2
Arbitrarily Shaped
Flat Sample

passing a current I_2 into B and out of C and measuring the potential difference V_2 between V_A and V_D ($V_2 = V_A - V_D$).

He derived the following formula to determine the resistivity, using these resistance measurements.

$$\rho = \frac{\pi t}{\ln 2} \frac{(R_1 + R_2)}{2} f\left(\frac{R_1}{R_2}\right) \quad (16)$$

where t is the thickness of the sample and the value of the function $f(R_1/R_2)$ is obtained from the following:

$$\frac{Q-1}{Q+1} = \frac{f}{\ln 2} \operatorname{arccosh}\left(\frac{1}{2} \exp\left(\frac{\ln 2}{f}\right)\right) \quad (17)$$

where $Q = R_1/R_2$ or its reciprocal so that $Q \geq 1$, and $f = f(R_1/R_2)$.

2.3 Measurements

The resistance measurements were made in two configurations, as shown in Figure 3, with $I=200 \mu\text{A}$. This covers all four sides and contacts. The measurements were repeated after reversing the current.

The resistivity was calculated for each configuration and if the resistivities did not agree within 10%, the data at that temperature was discarded. When inconsistencies occurred, they did so only at low temperatures, possibly due to the probe tip not making good contact.

The Hall voltage is determined by forcing a current into A and out of C and measuring the potential developed

across B and D, both in the absence and in the presence of a uniform magnetic field H perpendicular to the surface of the test specimen. The change in the developed

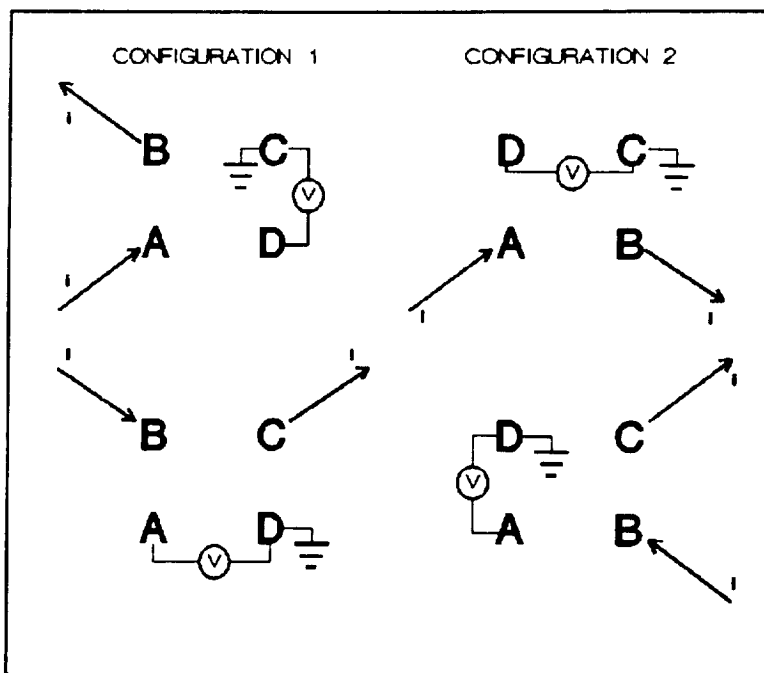


Figure 3 Resistivity Configurations

voltage across B and D from when the magnetic field is absent to when it is present, is the Hall voltage V_H . Equation (9), used to calculate the Hall coefficient is repeated here.

$$R_H = \frac{t}{B I} V_H \quad (\text{cm}^3/\text{C}) \quad (18)$$

The current I was 1 mA and the magnetic flux density B was 5000 gauss. Readings were repeated after reversing the current. No heating effects were observed. The Hall magnet and power supply did not allow the magnetic field to be reversed.

2.4 Activation Energy from Carrier Concentration

The derivation of the equations used to determine the activation energy from the carrier concentration data is presented for both cases, namely, where the dopant impurity is assumed to give rise to 1) a single localized energy level (single level model), 2) two distinct localized energy levels (double level model) in the forbidden band. The derivation assumes non-degenerate compensated material. If the donor impurity site has a bound electron it is assumed electrically neutral regardless of the state of the electron, namely, the ground state or an excited state [54].

The following derivations will be done for n-type materials since the form of the equations for p-type material is the same, except that β , the degeneracy factor³, is usually larger than one [54].

2.4.1 Single Level Model

The form of the equation for a compensated material is [54]

$$n + N_a^- = \frac{N_d}{1 + \beta^{-1} \exp(\epsilon_d + \eta)} \quad (19)$$

³ $\beta = 0.5$ for donors and $\beta = 2$. for acceptors was used.

where n is the electron concentration, N_a^- is the density of ionized acceptors, and N_d is the total density of donors. The constant β is the spin degeneracy factor and depends on the number of ways an electron can occupy a given level. The reduced activation energy $\epsilon_d = E_d/kT$, and the reduced Fermi energy $\eta = E_f - E_c/kT$. Here E_d is the activation energy which is the same as the donor ionization energy $E_c - E_{\text{donor}}$, and E_f , E_{donor} and E_c are Fermi energy level, donor energy level and the conduction band edge, respectively.

Assuming 100% ionization for the minority dopant acceptors, equation (19) can be rewritten as

$$(n + N_a) (1 + \beta^{-1} \exp(\epsilon_d + \eta)) = N_d \quad (20)$$

Since, for a non-degenerate case $\exp(\eta) = n/N_c$, where N_c is the effective density of states⁴ in the conduction band,

$$(n + N_a) \left(1 + \frac{n}{\beta N_c} \exp(\epsilon_d)\right) = N_d \quad (21)$$

Multiplying out the left side of this equation and combining terms gives

⁴ N_c depends on the density of states effective mass of electrons, m_{de}^* . Appendix E gives a detailed discussion of the effective mass of electrons and holes in 6H-SiC. In the data reduction $m_{de}^* = 0.915 m_0$ and the density of states effective mass of holes $m_{dh}^* = 1.0 m_0$.

$$n^2 \left[\frac{1}{\beta N_c} \exp(\epsilon_d) \right] + n \left[1 + \frac{N_a}{\beta N_c} \exp(\epsilon_d) \right] + [N_a - N_d] = 0 \quad (22)$$

Dividing through by n^2 and solving for $1/n$ using the quadratic formula gives

$$\frac{1}{n} = \frac{- \left[1 + \frac{N_a}{\beta N_c} \exp(\epsilon_d) \right] - \sqrt{\left[1 + \frac{N_a}{\beta N_c} \exp(\epsilon_d) \right]^2 - 4 \frac{(N_a - N_d)}{\beta N_c} \exp(\epsilon_d)}}{2 (N_a - N_d)} \quad (23)$$

Therefore,

$$n = \frac{2 (N_d - N_a)}{\left[1 + \frac{N_a}{\beta N_c} \exp(\epsilon_d) \right] + \sqrt{\left[1 + \frac{N_a}{\beta N_c} \exp(\epsilon_d) \right]^2 + \frac{4 (N_d - N_a)}{\beta N_c} \exp(\epsilon_d)}} \quad (24)$$

which is the equation used in the least squares analysis (Appendix C). E_d , N_d and N_a are the parameters solved for by an iterative method.

2.4.2 Double Level Model

The general form of the equation for compensated material is given by

$$n + N_a = \sum_{j=1}^m \frac{N_{d_j}}{1 + \beta_j^{-1} \exp(\epsilon_{d_j} + \eta)} \quad (25)$$

which gives the following cubic equation in n for the double level analysis ($m=2$).

$$n^3 \left[\frac{\exp(\epsilon_{d_1} + \epsilon_{d_2})}{\beta_1 \beta_2 N_c^2} \right] + n^2 \left[\frac{\exp(\epsilon_{d_1})}{\beta_1 N_c} + \frac{\exp(\epsilon_{d_2})}{\beta_2 N_c} + \frac{\exp(\epsilon_{d_1} + \epsilon_{d_2})}{\beta_1 \beta_2 N_c} \right] + n \left[1 + \frac{N_a - N_{d_2}}{\beta_1 N_c} \exp(\epsilon_{d_1}) + \frac{N_a - N_{d_1}}{\beta_2 N_c} \exp(\epsilon_{d_2}) \right] + [N_a - N_{d_1} - N_{d_2}] = 0 \quad (26)$$

The Italian mathematician Girolamo Cardano [55] found the closed form solution for a cubic of the form

$$x^3 + px + q = 0 \quad (27)$$

to be

$$x = -\frac{A+B}{2} \pm \frac{A-B}{2} \sqrt{-3} \quad (28)$$

where

$$A = \sqrt[3]{-\frac{q}{2} + \sqrt{\frac{q^2}{4} + \frac{p^3}{27}}} \quad (29)$$

$$B = \sqrt[3]{-\frac{q}{2} - \sqrt{\frac{q^2}{4} + \frac{p^3}{27}}}$$

Equation (26) can be expressed as

$$\frac{1}{n^3} + \frac{a}{n^2} + \frac{b}{n} + c = 0 \quad (30)$$

and it can be made to resemble equation (27) by substituting

$$\frac{1}{n} = \left(x - \frac{a}{3}\right) \quad (31)$$

into the above cubic equation.

This gives

$$p = \left(b - \frac{a^2}{3}\right) \quad (32)$$

and

$$q = \frac{2a^3}{27} - \frac{ab}{3} + c \quad (33)$$

Substituting equations (32) and (33) in equation (29) and the resulting values of A and B in equation (28), we can solve for n from equation (31).

The values: 1) N_{d1} , N_{d2} , the doping concentrations corresponding to the two ionization (activation) energy levels E_{d1} and E_{d2} respectively, 2) E_{d1} , E_{d2} , and 3) N_a are obtained iteratively from a least-squares fit of the temperature-dependent carrier concentration data.

2.5 Activation Energy from $n(T)$ and $\rho(T)$ at low Temperatures.

Equation (21) for n is repeated here

$$(n+N_a) \left(1 + \frac{n}{\beta N_c} \exp(\epsilon_d)\right) = N_d \quad (34)$$

With $N_a = 0$ and at low temperatures, where $kT \ll E_d$, equation (34) can be approximated as [56]

$$n = \sqrt{\beta N_c N_d} \exp\left(\frac{-E_d}{2kT}\right) \quad (35)$$

Hence, E_d can be found from the slope of $\ln(n)$ vs $1/T$ at low temperatures.

Equation (13) for the resistivity is repeated here

$$\rho = \frac{E}{J} = \frac{E}{n q v_d} \quad (36)$$

Substituting Eq. (35) into Eq. (36) gives [46]

$$\rho = \frac{E}{q v_d} \frac{\exp\left(\frac{E_d}{2kT}\right)}{\sqrt{\beta N_c N_d}} \quad (37)$$

Again, E_d can be found from the slope of $\ln(\rho)$ vs $1/T$ at low temperatures.

In equation (35) and (37), the temperature dependence of the exponential factor completely masks the temperature dependence of the pre-exponential factor. Hence, the pre-exponential factor can be treated as a constant with respect to the temperature.

2.6 Measurement Accuracy

2.6.1 Error Due to Contact Size

A systematic error is introduced in the measurements when the sizes of the contacts are not negligible in comparison with the dimensions of the sample. By estimating the error [47], a correction factor can be applied to the results. For the samples used in this research these corrections were not a factor.

2.6.2 Calculation of Error in the Final Result

During a measurement, the voltmeter (Fluke 8520A) had the capability of being programmed to take multiple readings and do a statistical analysis. The t-distribution was used to obtain the uncertainty in the sample standard deviation s_x . The confidence limits on the measurements x are $\pm t_{\alpha, \phi} s_x$, where α represents the confidence level (i.e. 90%, 95%, 99%) and $\phi = n-1$ is the degree of freedom in the measurement, where n is the number of measurements. There were 61 measurements so for the 95% confidence level $\alpha = .025$ and $t_{.025, 60} = 2$.

The error propagation was calculated from the initial measurements to the final calculated result. Since the variance on the primary inputs, the thickness and the

voltage, was known the variance on the results could be calculated, using the following relationship from [48]:

$$V_r = \left(\frac{\partial r}{\partial t}\right)^2 V_t + \left(\frac{\partial r}{\partial v}\right)^2 V_v \quad (38)$$

As an example, to find the confidence limits on the carrier concentration n , where n is defined by

$$n = \frac{I_H}{(q R_H)} = \frac{a}{R_H} \quad (39)$$

and a stands for r_H/q . Then

$$\frac{\partial n}{\partial R_H} = -\frac{a}{R_H^2} = -\frac{n}{R_H} \quad (40)$$

so that from equation (38)

$$V_n = \left(-\frac{n}{R_H}\right)^2 V_{R_H} \quad (41)$$

To calculate V_{R_H} , the variance in R_H , we first express R_H as

$$R_H = \frac{v_H t}{B I} = a v_H t \quad (42)$$

where a stands for $(1/BI)$.

$$\frac{\partial R_H}{\partial v_H} = a t = \frac{R_H}{v_H} \quad (43)$$

$$\frac{\partial R_H}{\partial t} = a v_H = \frac{R_H}{t} \quad (44)$$

Then, using Eq. (38) gives us the following expression for V_{RH} , the variance in R_H :

$$V_{R_H} = \left(\frac{R_H}{v_H}\right)^2 V_{v_H} + \left(\frac{R_H}{t}\right)^2 V_t \quad (45)$$

The final result for the variance on the carrier concentration is obtained when equation (45) is substituted into equation (41).

$$V_n = \left(-\frac{n}{R_H}\right)^2 \left[\left(\frac{R_H}{v_H}\right)^2 V_{v_H} + \left(\frac{R_H}{t}\right)^2 V_t \right] \quad (46)$$

Then, the standard deviation in n is given by

$$s_n = \sqrt{V_n} \quad (47)$$

and the limits on n for 95% confidence level are $n \pm 2s_n$.

The variance of the voltage, V_{vH} was calculated from voltmeter readings; V_t was determined as follows. The thickness of the $4\mu\text{m}$ epilayers was accurate within $\pm 1\mu\text{m}$. Although this was arrived at through many (hundreds of) observations, it was justified in letting ϕ equal 60. With this decision, $\pm t_{\alpha, \phi} s_t = \pm 2s_t = \pm 1\mu\text{m}$ so that $s_t = 0.5$ and

$V_t = 0.25$. This was used in the calculation of the confidence limits on the resistivity ρ , carrier concentration n , and Hall mobility μ_H . Figures 4 through 7 show n plotted against reciprocal temperature. At each temperature, the variance in n is indicated by an error bar.

The voltmeter and electrometer were considered accurate. The voltmeter error was approximately $\pm 0.012\%$ on the 100mV scale, and the electrometer error was $\pm 0.5\%$ on the 10^{-3}A scale.

2.7 Extraneous Effects

The measurements can be influenced by thermoelectric and thermomagnetic effects besides the galvanomagnetic effect we are trying to measure.

The thermoelectric effects are the Seebeck and Peltier effects. The Seebeck effect is the effect produced by a hot-point probe where the mobile charge carriers move away from the higher temperature area. Both the type and quantity of charge can be measured as in the Hall effect. The voltage produced by the Seebeck effect is $V_s = -\alpha_0 \Delta T$, where α_0 is the thermoelectric coefficient and ΔT is the temperature difference. This voltage can be measured and accounted for while making the Hall voltage and resistivity voltage measurements.

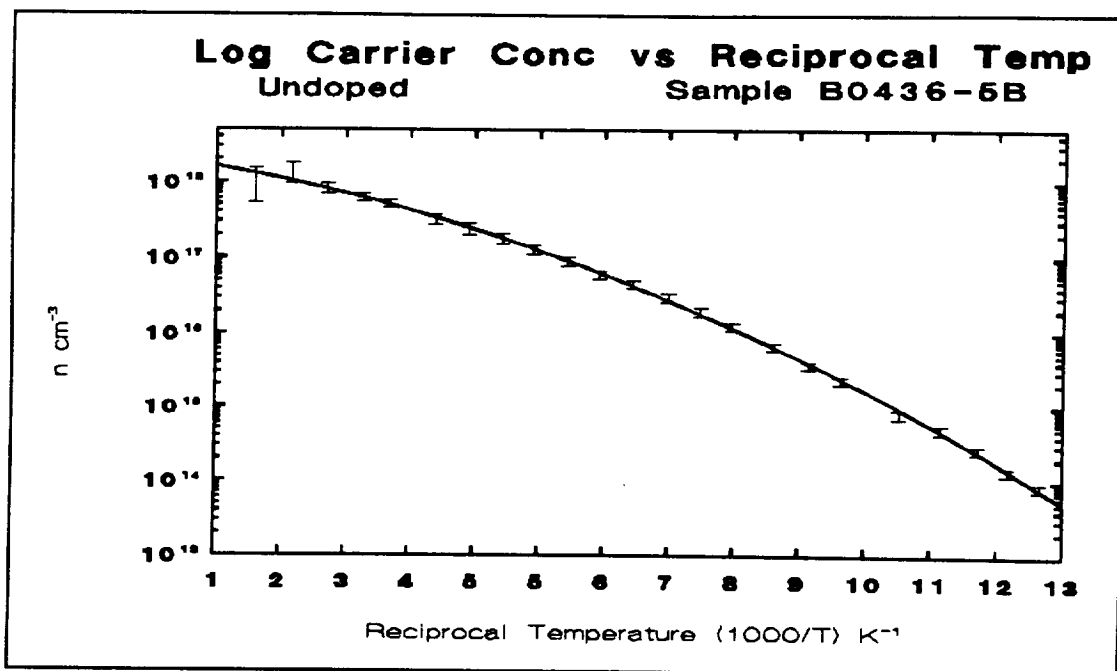


Figure 4 Carrier concentration as a function of temperature for the undoped Cree substrate B04365-5B with error bars.

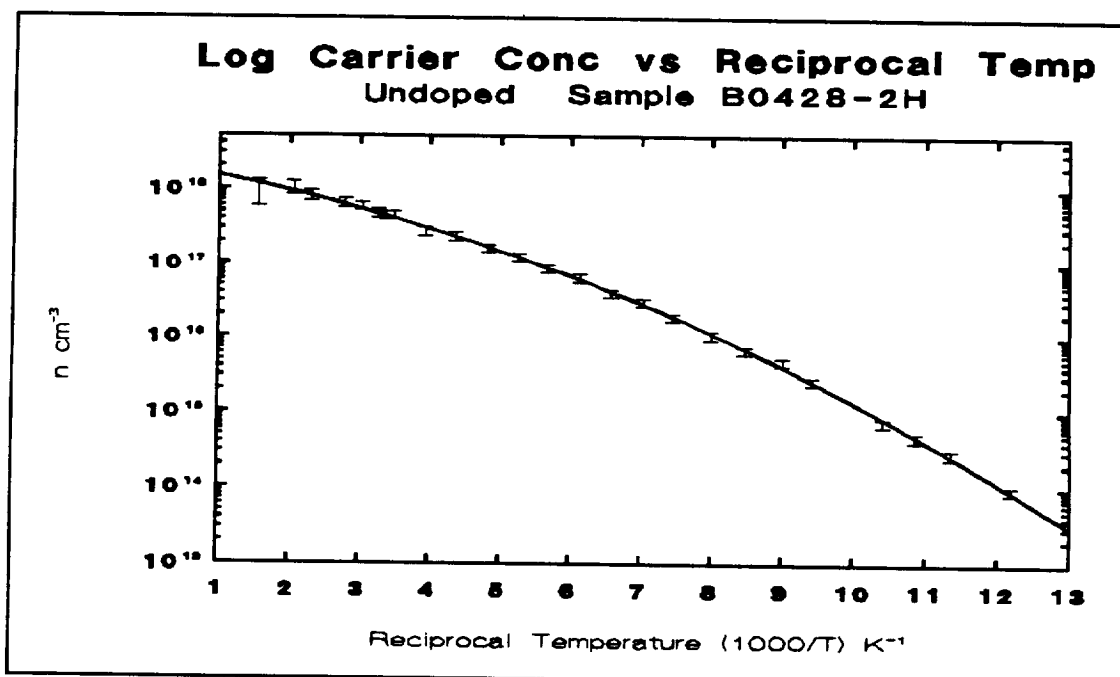


Figure 5 Carrier concentration as a function of temperature for the undoped Cree substrate B0428-2H with error bars.

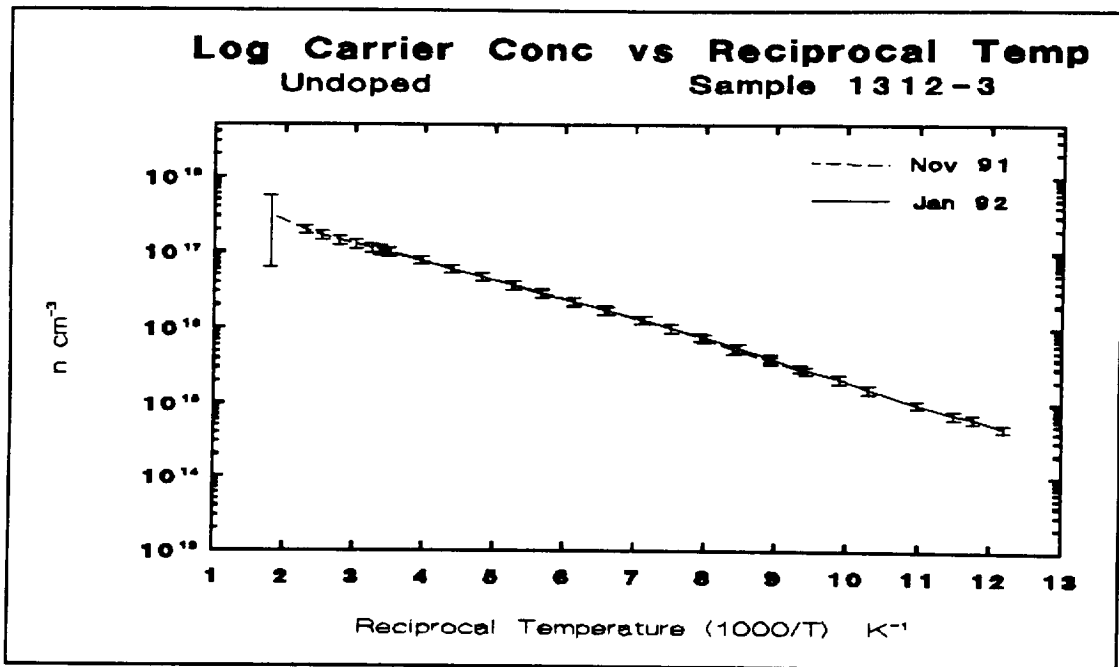


Figure 6 Carrier concentration as a function of temperature for the undoped NASA grown epilayer 1312-3 with error bars.

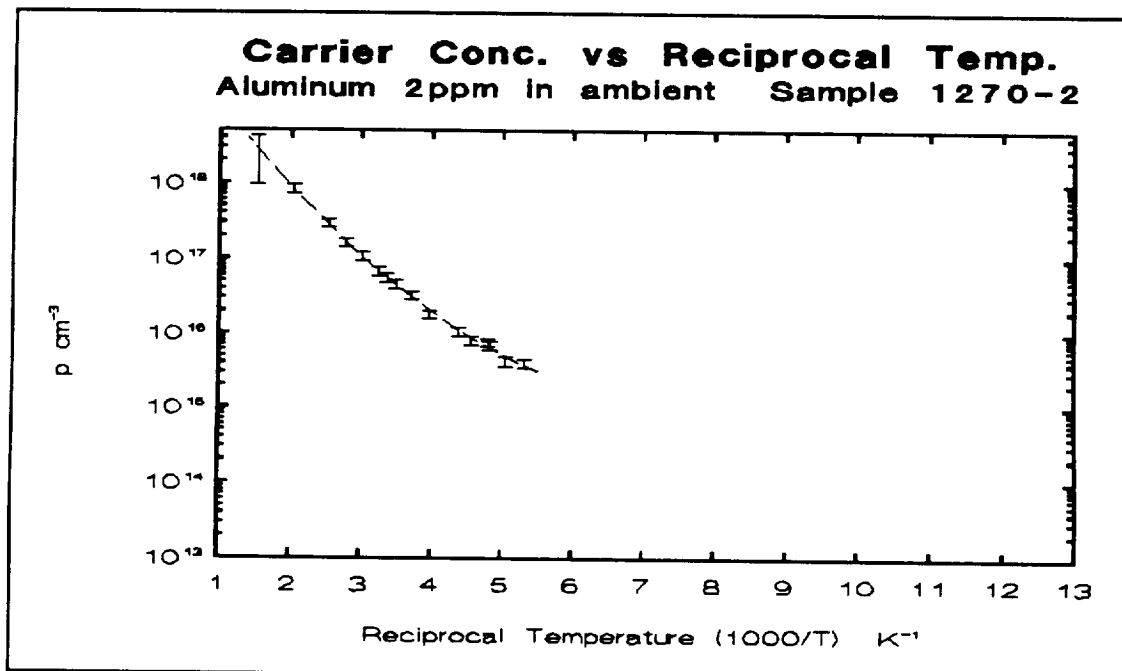


Figure 7 Carrier concentration as a function of temperature for the aluminum doped NASA grown epilayer 1270-2 with error bars.

The Peltier effect results from the different amounts of heat that are carried by the current in different materials. If two materials with different Peltier coefficients are in intimate contact, the junction will either get warmer or cooler depending on the direction of the current and the difference between their Peltier coefficients. The magnitude of the current and the magnitude of the difference between the Peltier coefficients determines the magnitude of the heat current.

The net rate of increase of heat energy at the junction, per unit area of the junction, is given by

$$\Delta J_Q = J_{Q_1} - J_{Q_2} = (\pi_1 - \pi_2) J \quad (48)$$

Here the J_Q 's are the heat currents, the π 's are the Peltier coefficients of the two materials (π_1 is for the material the electric current is entering and π_2 is for the material that the current is leaving), and J is the electric current density.

If any temperature gradient in the sample is caused by this Peltier effect, then the resulting Seebeck voltage due to such a temperature gradient can be eliminated by reversing the sample current and taking the average of the resistive voltage readings across the sample.

The magnetoresistance is eliminated by taking a reading and reversing the direction of \mathbf{B} and taking another reading, then averaging the readings. The Nernst and Rigi-Leduc

effects can be eliminated in a similar way by reversing both **B** and **J** and averaging the readings. However, the Ettingshausen effect cannot be eliminated by reversing and averaging the measured voltages.

In short, all of the extraneous effects (with the exception of the Ettingshausen effect [44]) can be eliminated by reversing current and/or magnetic field as mentioned above.

Since in this research the magnetic field could not be reversed, the size of the effects need to be determined to see the magnitude of their influence on the measurements.

The references [3,9,46 and 49] were heavily relied upon for the equations used to calculate the magnitude of the influence of the thermoelectric and thermomagnetic effects.

In Table 1, the calculated values of the various extraneous voltages and temperature differences developed as a result of the thermoelectric and thermomagnetic effects for the 6H SiC undoped epilayer sample 1312-3 are presented at three different temperatures. As seen from this table, the magnitudes of the induced voltages and temperature differences are negligible.

Table 1 Calculated Thermo-(electric and magnetic) Effects

Undoped 6H-SiC epilayer sample 1312-3				
Temperature K		87	297	488
κ	W/cm K	35	4.9	2.4
κ_e	W/cm K	+3.627E-7	+1.759E-5	+1.326E-5
α_o	V/K	-2.107E-3	-1.833E-3	-1.847E-3
V_E	V	-6.333E-8	-1.907E-5	-2.959E-5
V_{ES}	V	-2.825E-11	-5.559E-11	-4.841E-11
V_N	V	+4.180E-6	+3.879E-7	+9.990E-8
ΔT_E	K	+1.341E-8	+3.033E-8	+2.621E-8
ΔT_S	K	+1.884E-9	+6.056E-8	+2.401E-8
$\Delta \rho$	Ω -cm	+1.566E-2	+1.348E-4	+8.945E-6

κ is the thermal conductivity

κ_e is the electronic thermal conductivity

α_o is the Seebeck co-efficient

V_E is the Ettingshausen voltage

V_{ES} is the Ettingshausen-Seebeck voltage

V_N is the Nernst voltage

ΔT_E is the Ettingshausen temperature difference

ΔT_S is the Righi-Leduc temperature difference

$\Delta \rho$ is the worst case error in the resistivity measurement

CHAPTER 3

SAMPLE PREPARATION

This chapter describes: 1) the 6H-SiC samples used in this research, 2) contact metalization, and 3) the design of a reactive ion etch mask to define the sample geometry.

3.1 Growth of 6H-SiC Epilayers

The 6H-SiC n- and p-type epilayers were grown by chemical vapor deposition (CVD), in the Engine Sensor Technology Branch of the NASA Lewis Research Center⁵. The 4 μ m epilayers⁶ were grown on 6H-SiC substrates, approximately 5.5 mm X 5.5 mm which were 3° off the crystallographic (0001) plane. The substrates were grown by the modified Lely method [40] by Cree Inc.

⁵ National Aeronautics and Space Administration, Lewis Research Center, 2100 Brookpark Rd., Brookpark OH 44135.

⁶The chemical vapor deposition (CVD) grown epilayers were made available to me for this research courtesy of Mr. J. Anthony Powell.

The test epilayers were always isolated from the substrate by a 4 μm thick buffer layer as shown in Figure 8. In order to obtain planar test epilayers, sample edges were trimmed with a wafering saw, because the buffer and test epilayers grow all around the substrate during the growth process. Reactive Ion Etch (RIE) patterning, if available, is a more convenient and more accurate method of defining sample geometry.

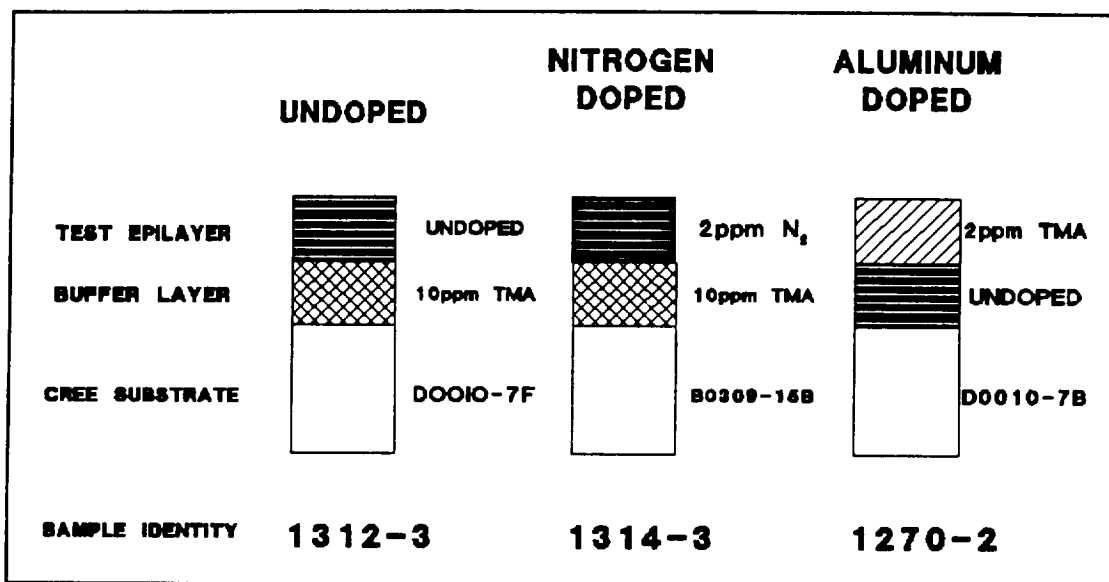


Figure 8 Epilayers

3.2 Contacts

A series of contacting schemes was tried using the materials Al, Au, Mo, Ni, Si, Ta, and Ti, either singly or in combinations. These materials were deposited either by evaporation or sputtering. Several of these schemes looked

promising. What was settled on for this research was aluminum for the p-type samples and nickel for the undoped and n-type samples. The contacts were Rapid Thermal Annealed (RTA) in forming gas (4% Hydrogen in Nitrogen) until they were determined to be ohmic.⁷ Generally, the anneal temperature was 925°C and the time was varied, from a few seconds to 1 or 2 minutes, to accomplish the anneal. It was observed that the n-type samples became a deeper green [1,8,41] after the RTA process.

It was noticed (during the trial and error process of finding the proper time/temperature combination for the RTA contacts) that if, for example, the aluminum contacts were overheated and the sample was etched to remove all remnants of the metalization, and if the new metalization overlapped areas where the old contacts had been, the new contacts were either already ohmic or required a very mild anneal to become ohmic. Even with these "mild", for SiC, annealing conditions, contrary to what is understood about the difficulty in doping SiC, it appears that doping had occurred, even if extending to only a few atomic layers.

⁷I would like to express my thanks to Carl Salupo for his assistance in the metalization and annealing processes.

3.3 Mask

Although not used in this research, a mask set was designed for Reactive Ion Etching (RIE) of van der Pauw patterns and Hall bars on the SiC samples for electrical characterization studies. The mask had two Hall bars and two van der Pauw patterns within a 2mm X 2mm square as shown in Figure 9.

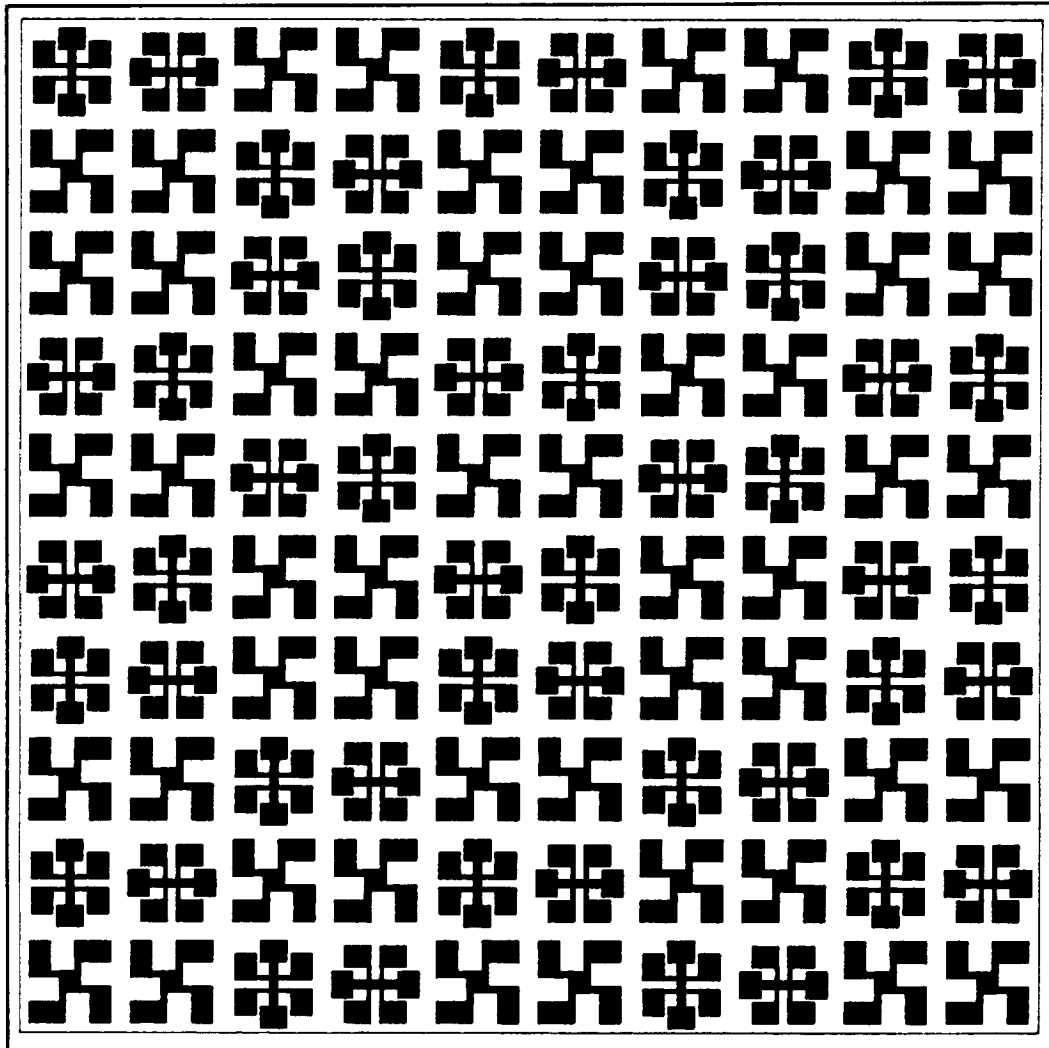


Figure 9 Mesa Mask Layout

The mask set was designed to reduce the measurement errors caused by contact size and placement (i.e. the contacts not being infinitesimally small and not being on the periphery of the sample [42]).

Two primary sources used for the design criteria of the Hall bars and van der Pauw patterns were Laboratory Notes on Electrical and Galvanomagnetic Measurements [43] for the orthogonal pin-wheel van der Pauw pattern dimensioning, and The American Society for Testing and Materials (ASTM) Designation:F76-86 [44] for the six contact Hall bar dimensioning.

There are two objectives that need to be balanced in the design, namely, the dimension ratios to reduce the errors caused by contact placement and the dimension ratios to account for the range of material resistivities that will be encountered. For example, in the van der Pauw pattern, as seen in Figure 10, the pin-wheel leg length (A) needs to be long compared to the sample area dimension (S), and the leg width (B) needs to be small compared to this same area dimension (S). As either ratio moves in the indicated direction the

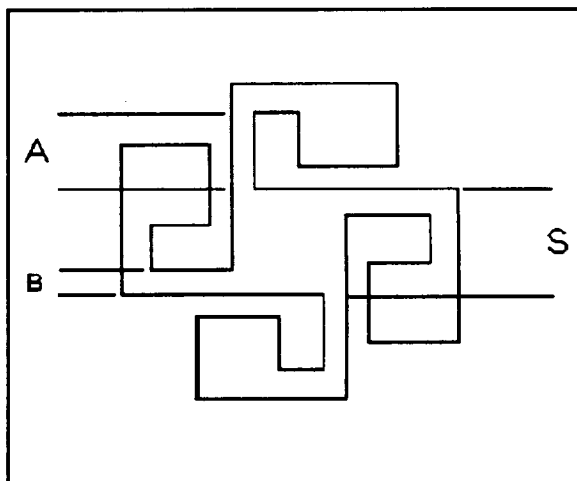


Figure 10 RIE Pin-wheel Pattern

measurement error decreases [43], but as the resistivity of the material increases these ratios need to move in the opposite direction to reduce heating effects.

The actual dimensions of the test patterns (Figures 11, 12) took into consideration the above-mentioned dimension ratios as well as the minimum area needed for the wirebonding pad size and the capabilities of the clean room photolithography environment which determines the minimum attainable line width.

We next consider how the upper limit of sustained current flow through a sample relates to pattern dimensions. What should the input power limitation be when measuring SiC epilayers so that the temperature rise in the specimen is limited to 0.5°C? Note that ASTM allows a ±1°C.

We know the power (P) dissipated by the sample is

$$P = I^2 \frac{\rho L_1}{A_1} \quad (49)$$

where I is the current through the sample, ρ is the resistivity of the specimen, L_1 is the length of the current carrying leg, and A_1 is the cross sectional area of current flow. We also know the heat flow through a sample per unit time is given by

$$P = \kappa A_2 \frac{\Delta T}{L_2} \quad (50)$$

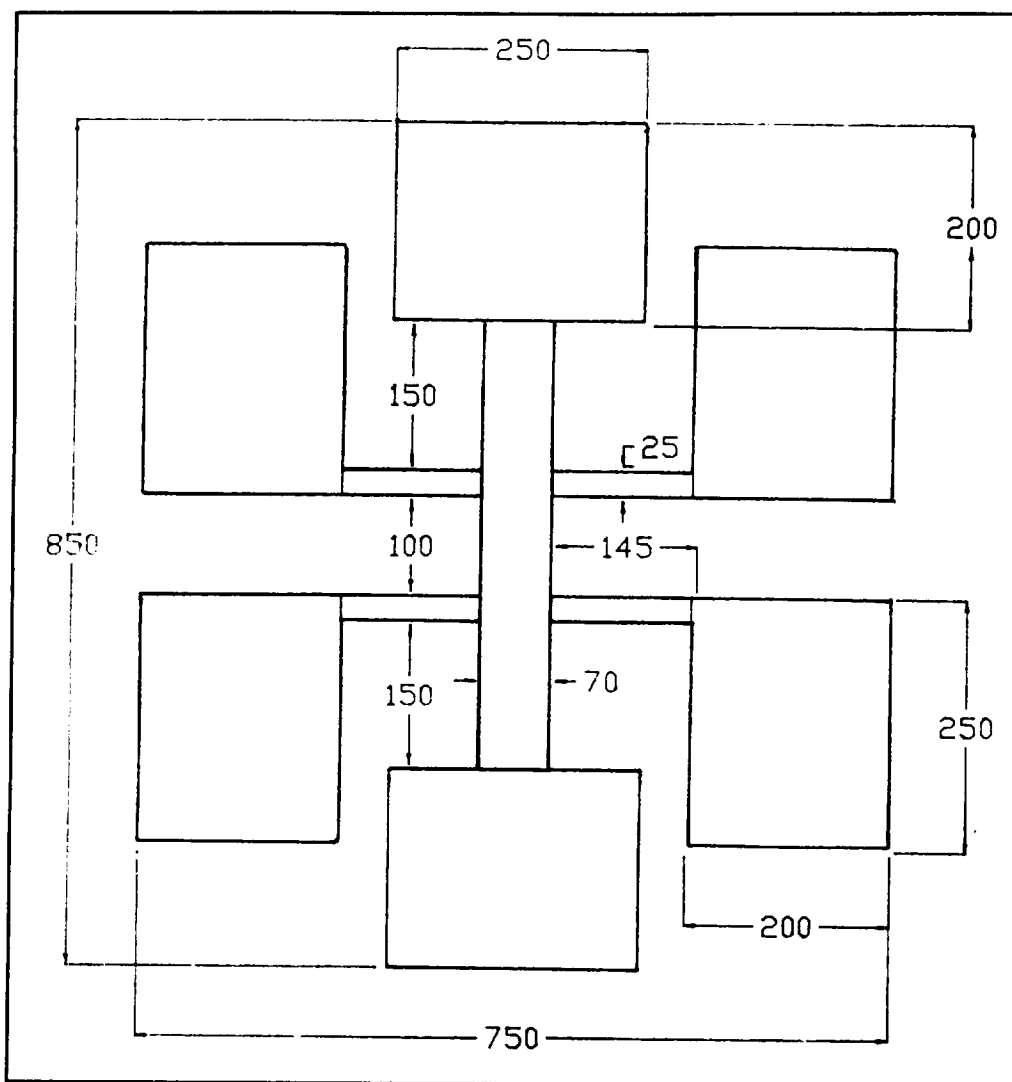


Figure 11 Dimensioned Hall Bar

where κ is the thermal conductivity, A_2 is the area for heat conduction in the sample, ΔT is the temperature difference, and L_2 is the length of the heat flow path, in this case $t/2$.

Combining Eq.(49) and Eq.(50) gives

$$I^2 \rho = \frac{\kappa A_1 A_2 \Delta T}{2 L_1 L_2} \quad (51)$$

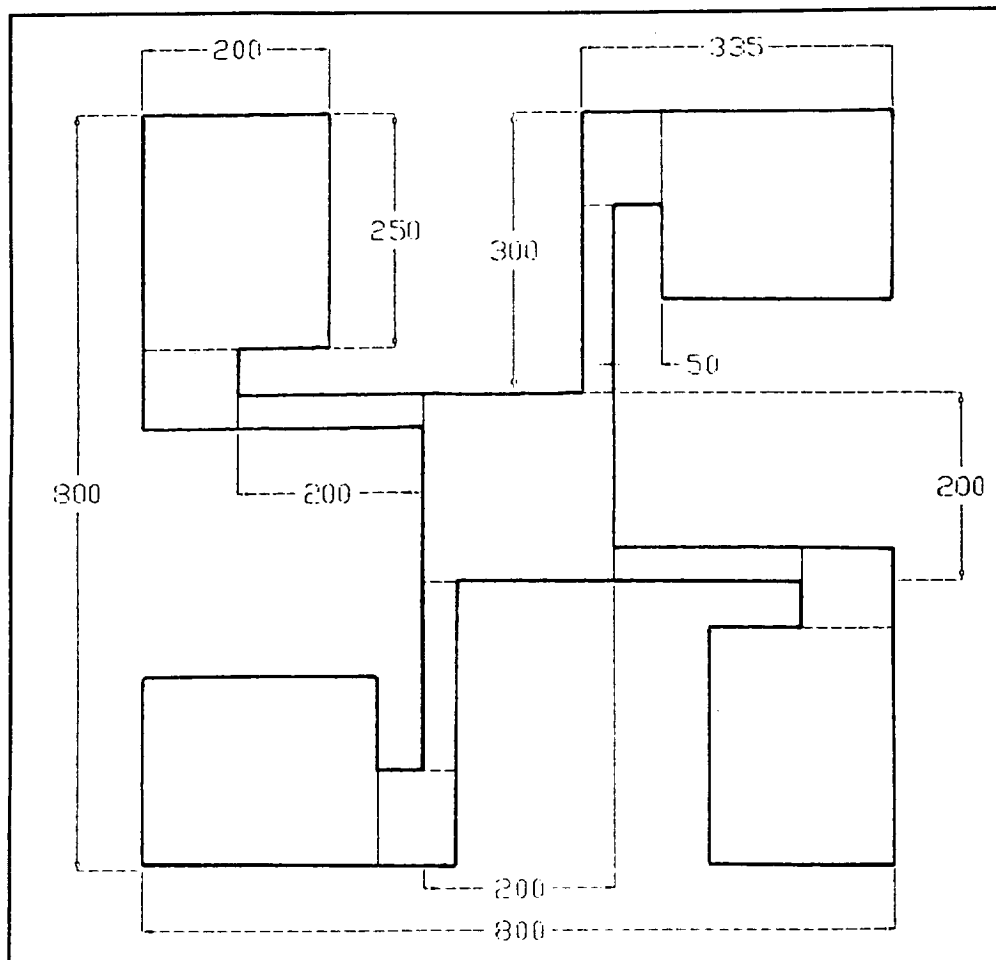


Figure 12 Dimensioned van der Pauw Pattern

for the van der Pauw configuration. The factor 2 in the denominator comes from the two current carrying legs of the sample. The leg dimensions will be the limiting factor in the design.

The areas are $A_1 = (w t)$ and $A_2 = 2(w L_1)$, where the factor 2 on the right hand side of A_2 is because the heat will be dissipated through both the top and bottom of the legs. Here w is the width of the current carrying leg (35 microns for the van der Pauw and 70 microns for the Hall bar patterns, as shown in figures 11 and 12) and t is the

epilayer thickness. Substituting for A_1 , A_2 and L_2 in equation (51) gives, for the van der Pauw pattern

$$I^2\rho = 2\kappa w^2\Delta T \quad (52)$$

and for the Hall bar gives

$$I^2\rho = 4\kappa w^2\Delta T \quad (53)$$

Table 2 below gives values of I and ρ satisfying these equations for $\Delta T = 0.5$ K.

Table 2 Current and Resistivity Values for $\Delta T = 0.5$ K from Equations (52) and (53)

CURRENT μA	RESISTIVITY UPPER LIMIT ($\Omega\text{-cm}$)					
	van der Pauw $w = 35 \mu\text{m}$			Hall $w = 70 \mu\text{m}$		
	70 K	300 K	1000 K	70 K	300 K	1000 K
200	13E3	1500	330	10E4	12E3	2600
500	2100	240	53	16E3	1900	430
1000	520	60	13	4200	480	100

Table 3 below gives, at each temperature, of the five samples used in this research, the sample which had the highest resistivity and value of the resistivity.

Table 3 Highest Resistivity Encountered

Temperature K	ρ Ω -cm	Sample Number
82	132.7	B0428-2H
300	2.01	1270-2
650	0.82	1270-2

Comparing tables 2 and 3, it is easy to see that for the samples used in this research, the dimensions defined by the RIE patterns would cause the temperature rise to be significantly smaller than 0.5 K for the measuring current I in the range of $200\mu\text{A}$ to 1mA .

The mask set was designed and the masks were received. However, the RIE was unavailable for this research. So, the samples that were tested with a grown epilayer were trimmed with a wafering saw to eliminate the effects of growth encapsulation mentioned earlier. The samples were $5.5\text{mm} \times 5.5\text{mm}$ square and the contacts were placed in the corners of these samples. For these dimensions the temperature rise ΔT caused by the measuring current in the range of $200\mu\text{A}$ to 1mA should be orders of magnitude smaller than that calculated for the RIE patterns.

CHAPTER 4

APPARATUS

4.1 Hall Setup

The magnet was a Varian Associates 6" Hall magnet (V3701F) and its power supply (V-FR2603) was equipped with a magnetic field regulator.

The magnetic field was monitored with a rotating-coil gaussmeter⁸. This gaussmeter was calibrated to read 2.94kG using a standard magnet⁹ of 2938 gauss. The Hall measurements were done at 5kG.

For temperature-dependent Hall measurements, the temperature was measured with a type J thermocouple¹⁰

⁸ Rawson Electrical Instrument Co., Cambridge, Mass., type 820, number 17270.

⁹ Ibid

¹⁰ Type J thermocouples are iron-constantan.

in conjunction with a Doric Trendicator 400A. The thermocouple had a temperature range from -200 to +933 °C, and the Doric Trendicator gave a one degree celsius resolution for the temperature reading.

4.2 Cryostat and Sample Jig

It was necessary to design and build a cryostat and sample platform for temperature-dependent electrical measurements on the test samples. For the design, it was deemed necessary that the magnetic metal content be minimized. Most of the design was accomplished with available off-the-shelf materials.

The cryostat was fabricated from a firebrick¹¹, which was cut in half and machined to

1. provide areas for the sample platform, gas torch¹², sample test leads and thermocouples;
2. fit between the pole pieces of the Hall magnet, which had a 2" clearance.

Appendix D shows detailed schematics of the cryostat construction.

¹¹Nock Fire Brick Co., series K-23.

¹² GTE, serpentine gas/air heat torch part 014923.

The test jig was a miniature probing station comprised of the sample platform and probes as shown in Figure 13.

The sample platform was fabricated from Macor¹³, a machinable glass-ceramic. The probes were made from nonmagnetic stainless steel washers, with slotted center; spot welded to these was a short section of nonmagnetic stainless steel wire to which standard tungsten probing tips were spot

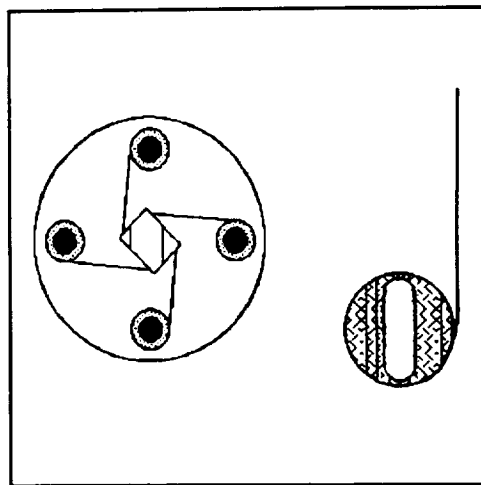


Figure 13 Sample Platform and Probe

welded. The probes provided three degrees of freedom.

4.3 Temperature Measurement & Control

There were two thermocouples, one in contact with the bottom of the sample and the other approximately 3mm above the sample platform. The two thermocouples were allowed to stabilize before a measurement was taken. The samples were extremely sensitive to temperature variations. For meaningful readings it was necessary that the temperature remained constant within $\ll \pm 1^\circ\text{C}$ during a measurement.

The low temperature measurements were controlled by adjusting the flow of nitrogen from a reservoir, which

¹³A product of Corning Glass Works, Corning, N.Y.

approximated an infinite source, through a coil immersed in liquid nitrogen.

For high temperature measurements, the voltage across the gas torch was controlled while nitrogen flow was kept constant.

4.4 Electrical Measurement

The remainder of the measurement apparatus consisted of a Fluke 8520A digital multimeter, used to measure the developed voltage, a Keithly Instruments 225 current source and a Keithly 616 digital electrometer, to measure current through the sample. These were connected to the sample through a switching box used to make the van der Pauw connections as shown in Figure 14. The square in the upper left corner

represents the sample to be evaluated, the letters (A, B, C, D) represent the contacts. The numbers on the lower portion of the figure

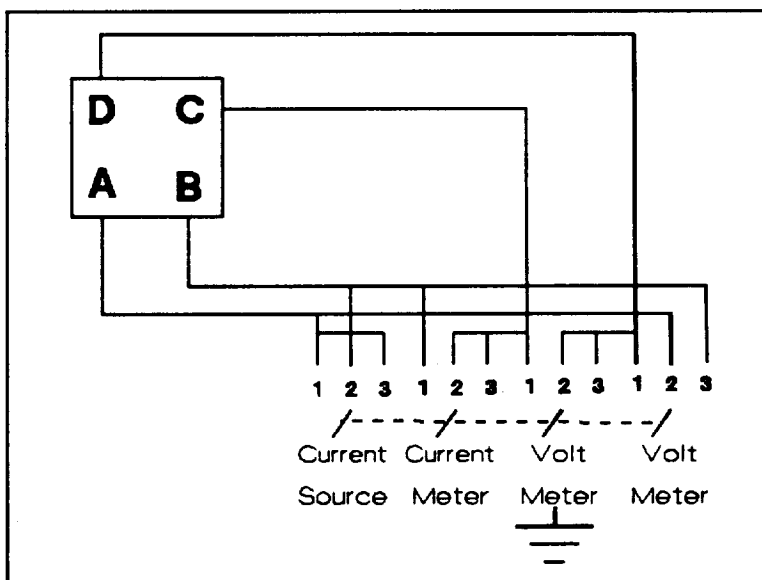


Figure 14 van der Pauw Connections

represent the possible switch positions; positions 1 and 2 are for resistivity measurements, position 3 is for the Hall measurement.

CHAPTER 5

Results and Discussion

In this chapter is presented: 1) a very brief historical background on the rise of silicon carbide to the point of being a viable semiconductor material for the fabrication of useful devices, 2) activation energies obtained by previous researchers using both the single and double activation energy level models, and 3) results of this research along with discussion, and 4) recommendations for future work.

5.1 Review of Past Work

The following historical information has been taken from [7], [8], and [9].

The semiconductor nature of silicon carbide was first investigated early in the twentieth century. Until 1955, the crystals used in investigations were results of chance occurrences from the commercial (Acheson) process of

manufacturing silicon carbide as an abrasive. Generally, neither the polytype¹⁴ nor the dopants were known for sure.

There was a thorough study made by Busch and Labhart in 1946 on Acheson crystals, and by Lely and Kröger in 1958 on crystals grown and doped by the process Lely published in 1955.

The Lely method was an attempt to produce purer crystals of known doping concentration on a laboratory scale. This was the impetus for the flurry of silicon carbide investigations that occurred during the sixties and the early seventies.

What finally raised silicon carbide to the place of being a viable material for device fabrication was the publication of two papers, [10] in 1981 and [1] in 1983, on what is called the modified Lely method.¹⁵ This brought about the present renewed interest in silicon carbide.

Results of Hall measurements on silicon carbide have generally been based on modeling SiC as either a single activation energy system or as a double activation energy system. These results are presented next.

¹⁴ See Appendix B.

¹⁵ See Appendix B.

5.1.1 Single Activation Energy Impurity Level System

S. H. Hagen and C. J. Kapteyns [16] determined the ionization energy of nitrogen donors in 6H-SiC that ranged from 0.081 to 0.095 eV depending on the dopant concentration.

Gerhard Pensl et al. [17] found an activation energy of 0.070 eV for heavily doped (low 10^{19} cm^{-3}) nitrogen implanted 6H-SiC samples.

T. Tachibana et al [18] found a donor ionization energy of 0.084 eV for undoped 6H-SiC.

Lomkina et al [15] found an activation energy of 0.095 eV for nitrogen donors in 6H-SiC with a dopant concentration of $\sim 1.3 \times 10^{17} \text{ cm}^{-3}$. For aluminum acceptors, they found an activation energy of 0.24 eV for an impurity concentration of $\sim 5.0 \times 10^{17} \text{ cm}^{-3}$.

Most authors reported values for the ionization energy of nitrogen ranging from 0.070 to 0.095 eV [7,9,15,18,19,20,21,22,23,24,25] and for aluminum from 0.190 to 0.280 eV [7,8,9,12,15,23,24,25,26,27,28].

5.1.2 Double Activation Energy Impurity Level System

The existence of more than one activation energy (Fig. 15), for dopants in 6H-SiC was explained in [11] and [29] by the fact that there are three inequivalent lattice sites for

impurity atoms. The number of inequivalent lattice sites is polytype dependent [11,23]; the larger the unit cell the more inequivalent sites present. The inequivalence

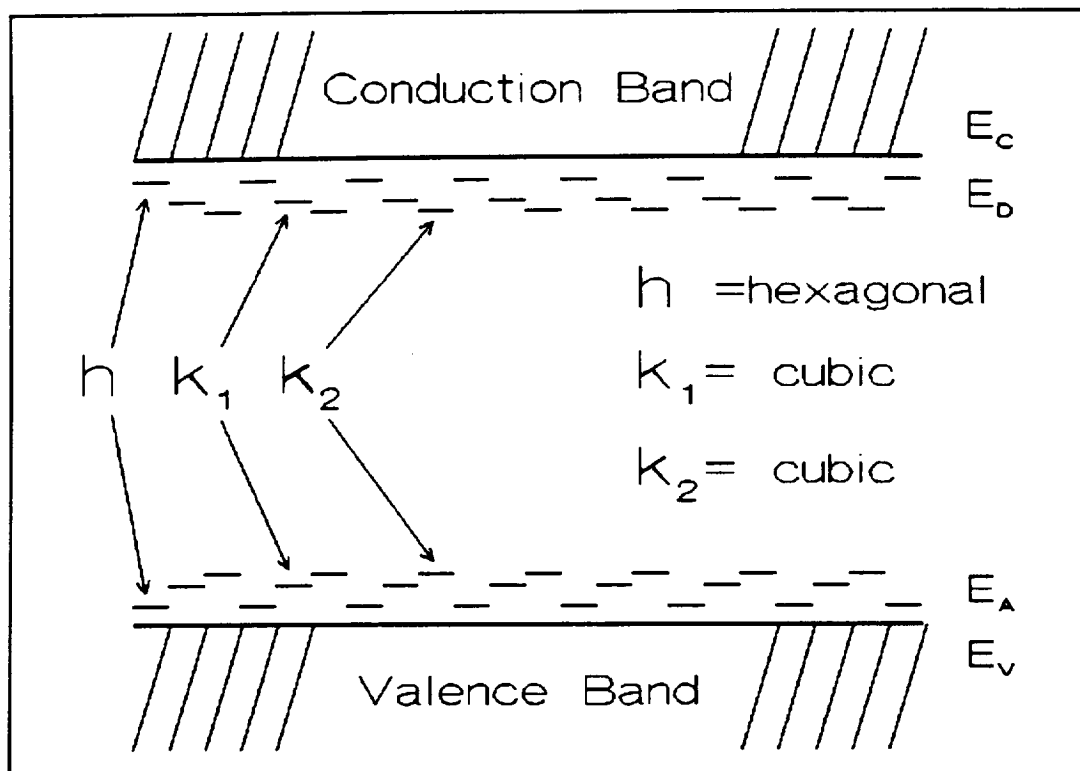


Figure 15 Energy Levels

manifests itself beyond the nearest neighbors [24] in the lattice stacking sequence.

The three inequivalent sites in 6H-SiC are categorized as a hexagonal site and two cubic sites. There is a larger binding energy difference between the hexagonal site and the two cubic sites (approximately 50-60 meV) [21,24,30,31,32,33] than between the two cubic sites themselves (approximately 5 meV) [21,30]. This justifies the use of the double activation energy model in spite of the fact that there exist three distinct activation energy

levels. Hall measurements have only resolved between the hexagonal and the two cubic sites, but has not resolved the levels between the cubic sites themselves.

These inequivalent energy levels do not conform, as many authors believe, to the unaltered hydrogen atom model [16,19,24,32]. A reason for this is that the hydrogen model does not distinguish between the inequivalent lattice sites [24]. There is also the difference caused by whether an impurity atom replaces silicon, as aluminum [29] ($E_g=0.27\text{eV}$) usually does, or replaces carbon, as nitrogen [19,29] ($E_g=0.15\text{ eV}$) and boron [19] ($E_g=0.39\text{ eV}$) do.

Table 4 shows, for nitrogen and aluminum in 6H-SiC, the activation energies that are obtained from electrical measurements using the two activation energy level model, along with the activation energies obtained optically.

5.2 Results and Discussion

There were five samples evaluated, two were virgin Cree substrates, and three were NASA-grown epilayers, one undoped, one n-type, and one p-type.

The n-type NASA epilayer sample 1314-3 was grown with 2 atoms of nitrogen per million of the host (Si and C) atoms in the ambient atmosphere of the growth chamber.

Table 4 Two Level Activation Energies

Nitrogen (eV)		Aluminum (eV)		Method	Ref
E_{dh}	E_{dc}	E_{ah}	E_{ac}		
0.075	0.135			optical	24
0.100	0.155	0.239	0.249	optical	23
0.101	(0.158, 0.163)			optical	21
0.080	0.130			electrical	21
0.096	0.142			electrical	32
0.100	0.150			electrical	33
0.081	(0.138, 0.142)			optical	30
0.080	0.120			electrical	30
0.086	0.125				
0.063	0.120			electrical	13
0.094	0.118				
0.085	0.119			electrical	14

E_{dh} is the hexagonal site donor activation energy.

E_{dc} is the cubic site donor activation energy.

E_{ah} is the hexagonal site acceptor activation energy.

E_{ac} is the cubic site acceptor activation energy.

The p-type NASA epilayer sample 1270-2 was grown with 2 aluminum atoms per million of the host (Si and C) atoms in the ambient atmosphere of the growth chamber.

All three undoped (at least, not intentionally doped) samples were found to be n-type from Hall measurements. The n-doped and p-doped epilayers were found to be n-type and p-type respectively.

Table 5 gives room temperature values of the electrical resistivity ρ , the majority carrier Hall mobility μ_H and the majority carrier concentration for the test samples.

Table 5 Room Temperature ρ , μ_H and carrier concentration for the test samples.

SAMPLE	SAMPLE Descrip.	SAMPLE TYPE	ρ Ω -cm	μ_H $\text{cm}^2/\text{V-s}$	Carrier Conc. cm^{-3}	
1	B0436-5B	Undoped Substrate	n-TYPE	.077	161.4	5.02e17
2	B0428-2H	Undoped Substrate	n-TYPE	.088	157.6	4.50e17
3	1312-3	Undoped Epilayer	n-TYPE	.250	235.8	1.06e17
4	1314-3	N ₂ -2ppm Epilayer	n-TYPE	.042	275.9	5.41e17
5	1270-2	Al-2ppm Epilayer	p-TYPE	.250	57.3	5.40e16

5.2.1 Single Activation Energy Level Analysis

Figures 16, 18, 20 and 22 show the carrier concentration versus T^{-1} for the two undoped Cree substrates, and the NASA grown undoped and NASA grown p-doped epilayers respectively. The solid line represents curve-fitting using equation (24), valid for the single level model. The fit is reasonably good for the two Cree undoped substrates B0436-5B (Figure 16) and B0428-2H (Figure 18). For the NASA grown undoped epilayer 1312-3 (Figure 20) the fit is reasonably good for low temperatures but the data diverge from the theory above room temperature. For the NASA grown p-doped epilayer 1270-2 (Figure 22) the fit is not very good above 500 K and below 200 K.

There was not enough data taken on the NASA grown n-type epilayer sample 1314-3 to do a meaningful analysis.

Table 6 gives the activation energy and the dopant concentrations N_d and N_a obtained from curve-fitting the temperature-dependent carrier concentration data to equation (24), valid for the single level model. For the activation energy, E_d of nitrogen, this research found a range of 0.078 eV to 0.101 eV as compared to the range of 0.07 eV to 0.095 eV reported in the literature. For aluminum, an activation energy E_a of 0.252 eV was found which is well within the range of 0.190 eV to 0.280 eV reported in the literature.

Table 6 Calculated Activation Energy and Impurity Concentrations from the Single Level Model.

Sample	Activation Energy & Doping Conc. from Temp. Dep. Carrier Conc. Single Level Model		Activation Energy from low temp	
			log $\rho(T)$	log $n(T)$
B0436-5B n-type	E_d N_d N_a	0.095 eV 1.54e18 cm ⁻³ 4.32e16 cm ⁻³	0.202 eV	0.247 eV
B0428-2H n-type	E_d N_d N_a	0.101 eV 1.55e18 cm ⁻³ 1.88e16 cm ⁻³	0.196 eV	0.225 eV
1312-3 n-type	E_d N_d N_a	0.078 eV 1.13e17 cm ⁻³ 1.99e14 cm ⁻³	0.097 eV	0.113 eV
1270-2 p-type	E_a N_a N_d	0.252 eV 4.57e18 cm ⁻³ 1.25e15 cm ⁻³	0.267 eV	0.243 eV

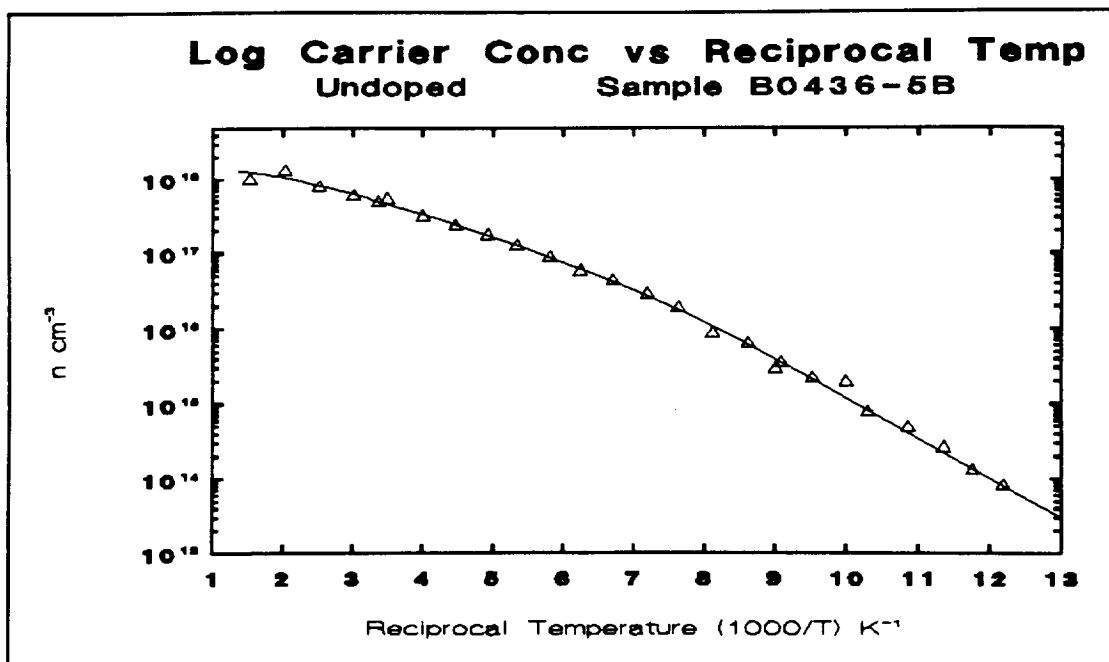


Figure 16 Carrier concentration as a function of temperature for the undoped Cree substrate B0436-5B.

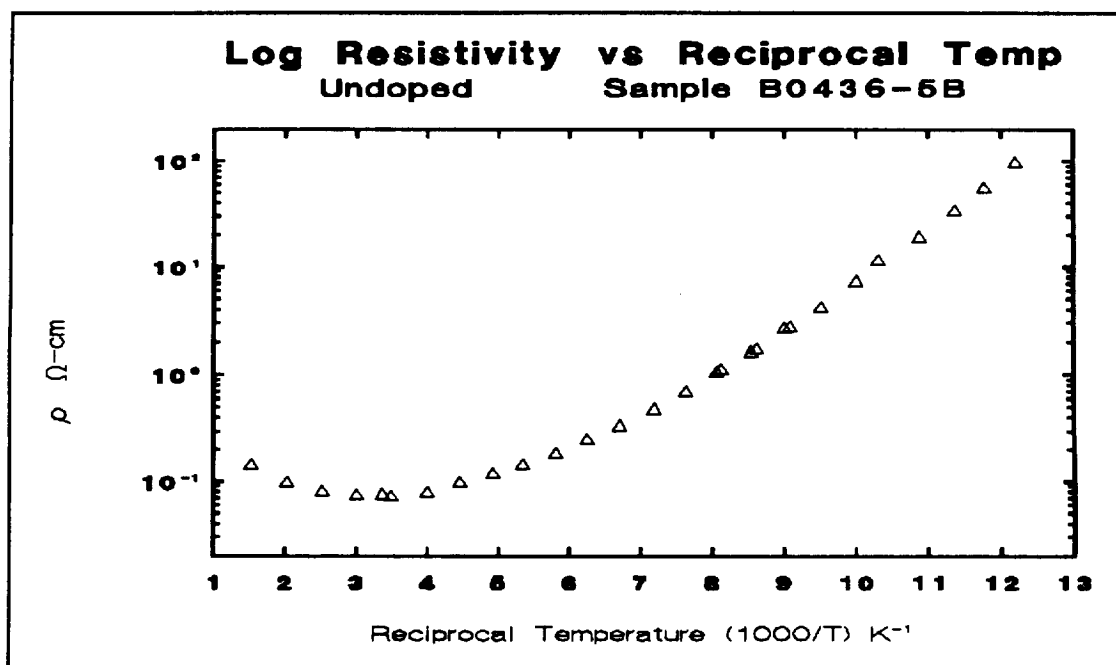


Figure 17 Resistivity as a function of temperature for the undoped Cree substrate B0436-5B.

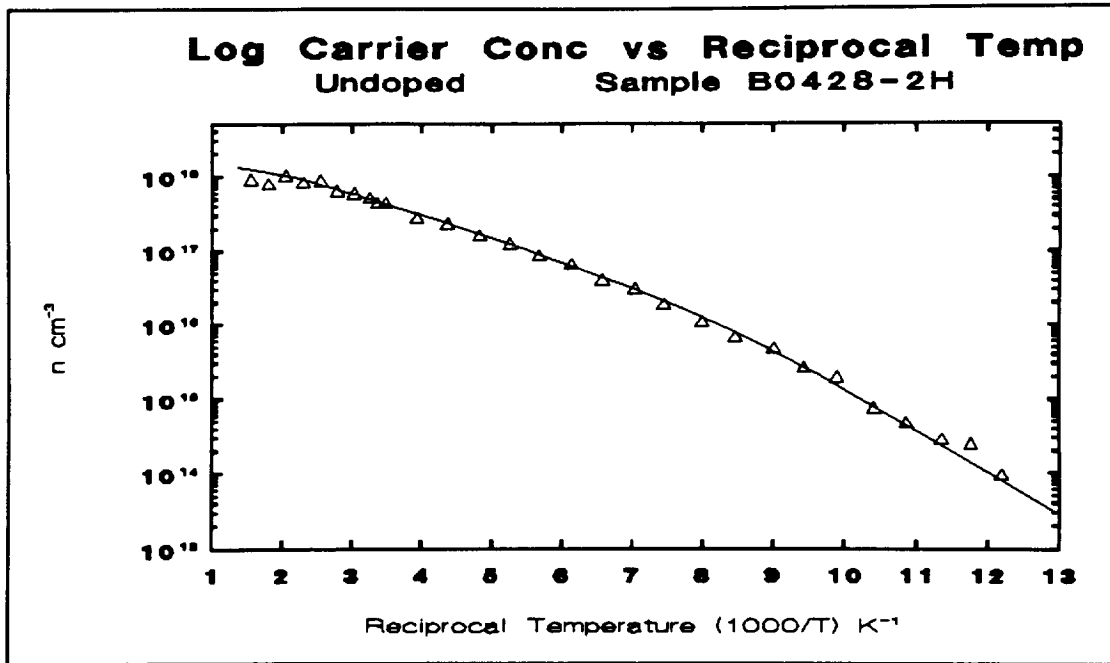


Figure 18 Carrier concentration as a function of temperature for the undoped Cree substrate B0428-2H.

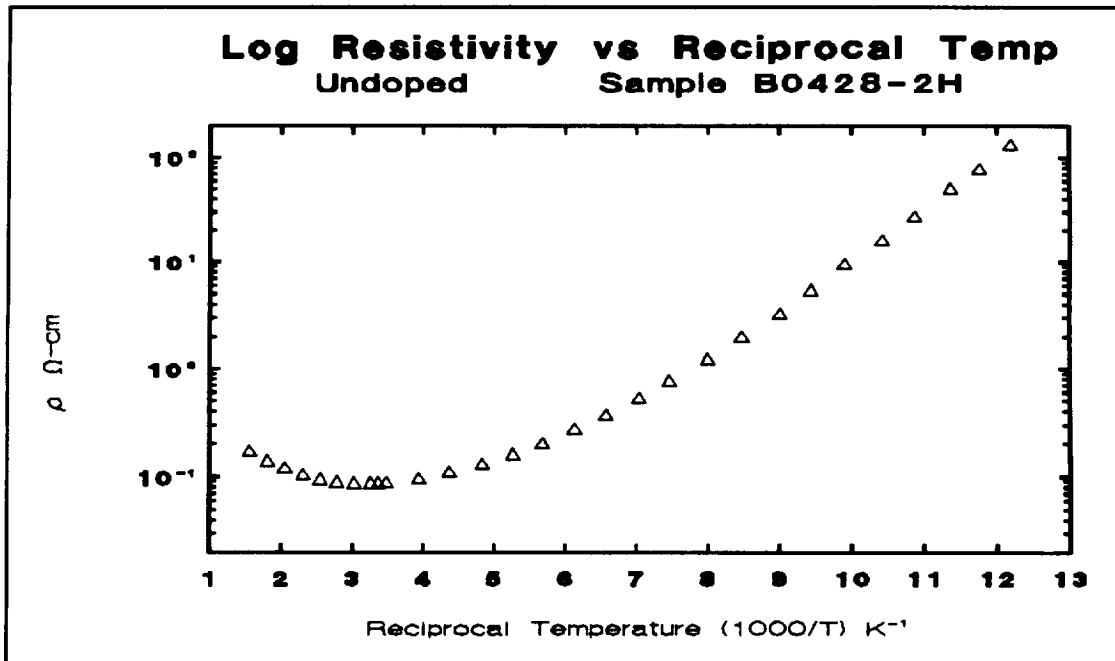


Figure 19 Resistivity as a function of temperature for the undoped Cree substrate B0428-2H.

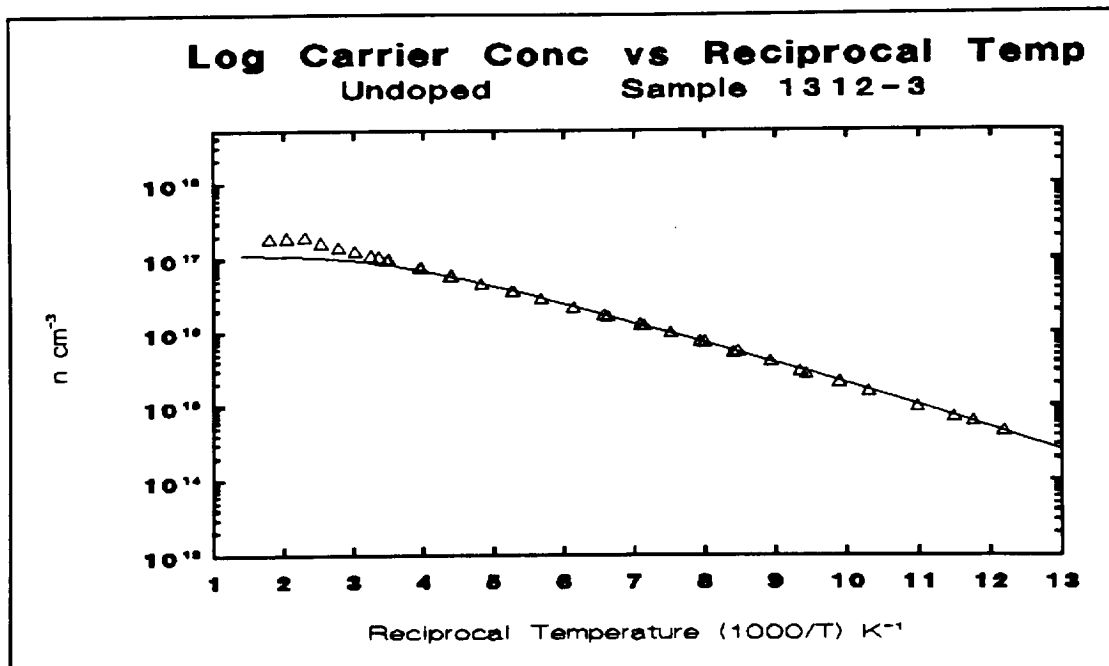


Figure 20 Carrier concentration as a function of temperature for the undoped NASA grown epilayer 1312-3.

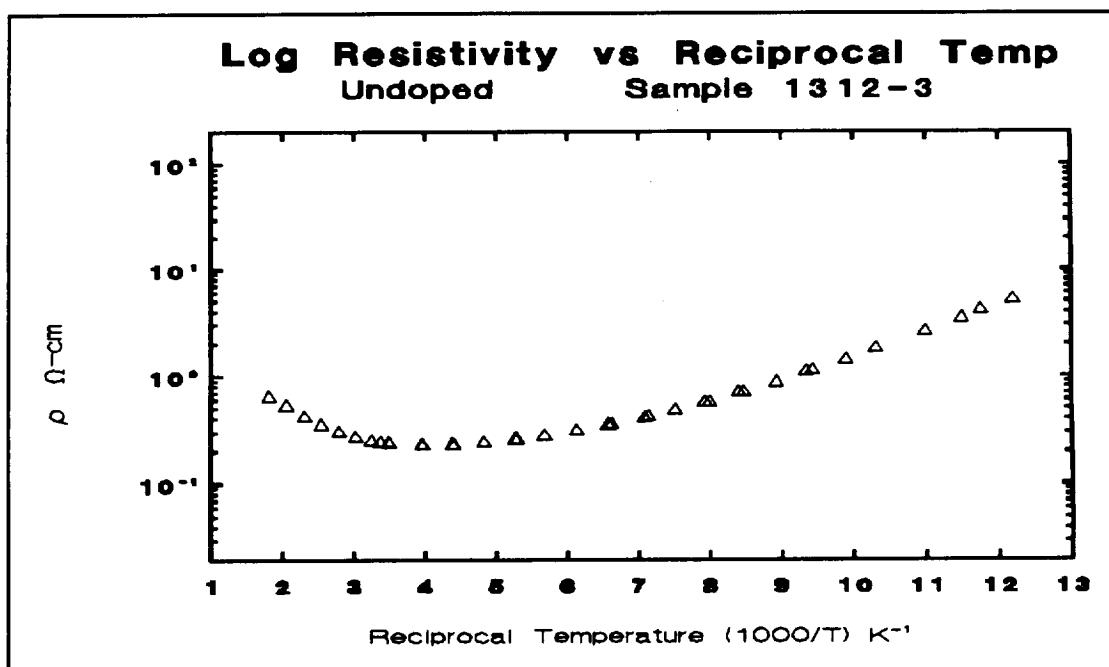


Figure 21 Resistivity as a function of temperature for the undoped NASA grown epilayer 1312-3.

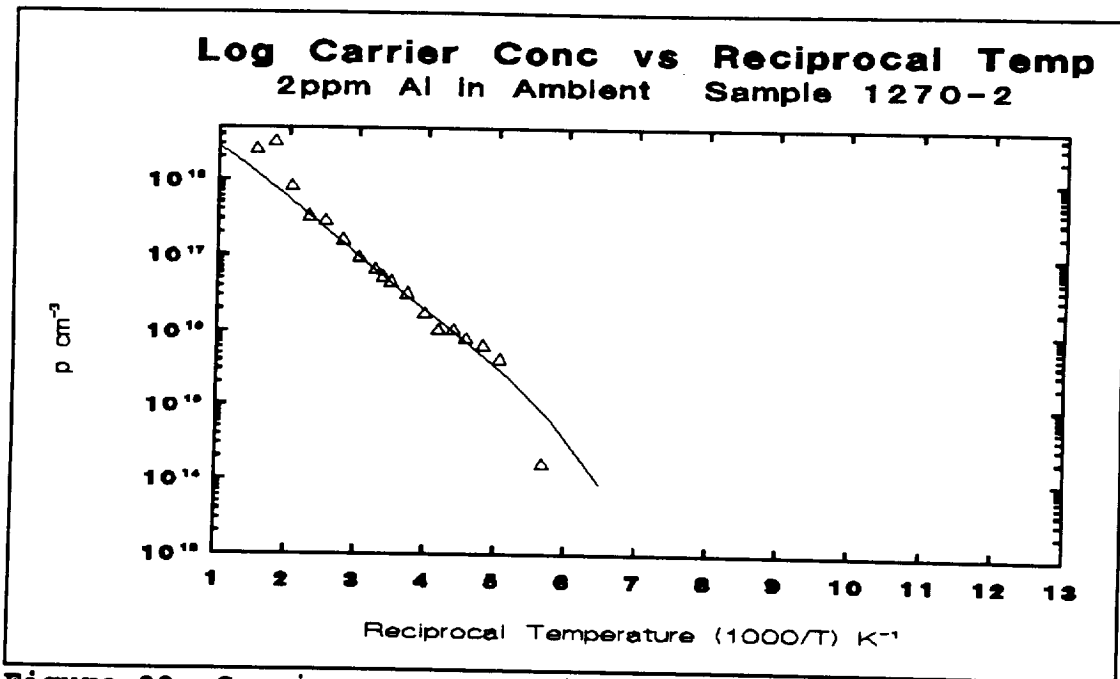


Figure 22 Carrier concentration as a function of temperature for the aluminum doped NASA grown epilayer 1270-2.

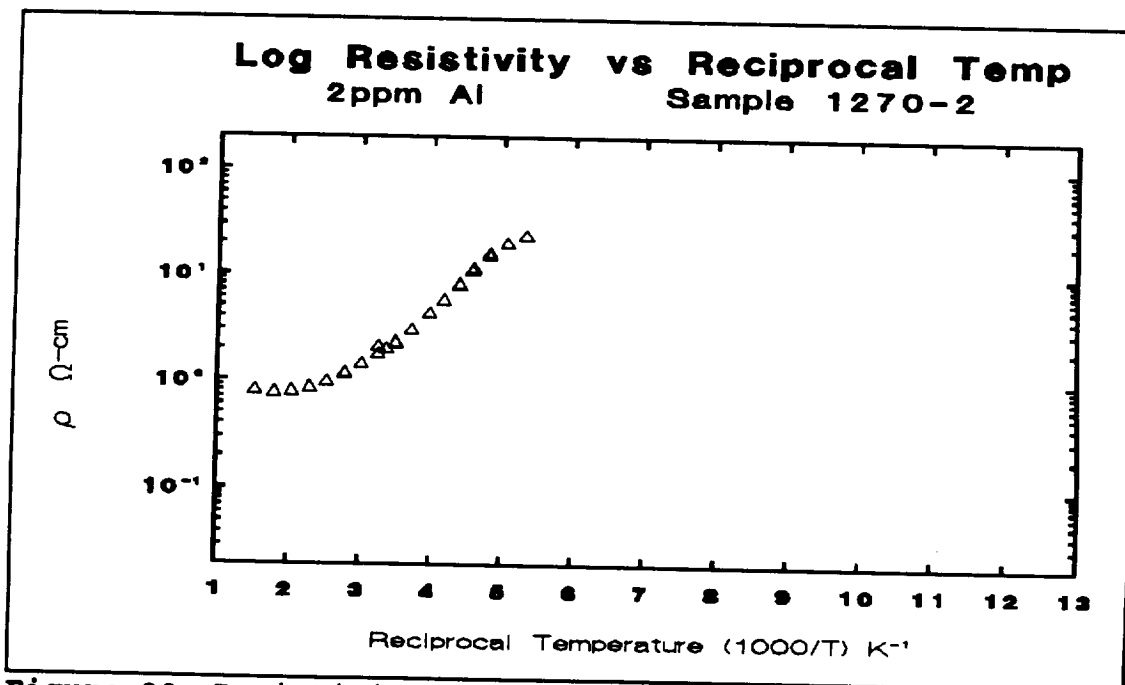


Figure 23 Resistivity as a function of temperature for the aluminum doped NASA grown epilayer 1270-2.

5.2.2 Results of Activation Energy From Low Temperature $n(T)$ and $\rho(T)$

The plots of $\log \rho$ versus $1/T$ for the two Cree substrate samples B0436-5B (Figure 17), B0428-2H (Figure 19) and the NASA grown undoped epilayer 1312-3 (Figure 21) look normal. The plot of $\log \rho$ versus T^{-1} for the NASA grown p-type epilayer 1270-2 does not appear as well behaved as the other three samples at low temperatures.

Table 6 also gives values of activation energies found from the slope of 1) low temperature $\log n(T)$ versus $1/T$ (Eq. (35)) and 2) low temperature $\log \rho(T)$ versus $1/T$ (Eq. (37)). As expected from equations (35) and (37), the activation energies obtained from low temperature $n(T)$ and $\rho(T)$ are in good agreement with each other. However, only for the p-type epilayer does the activation energy found this way agree with that found from fitting Eq. (24) to the carrier concentration data over the entire temperature range.

5.2.3 Double Activation Energy Level Analysis

In chapter 2, Eq. (26) relating the temperature dependent carrier concentration to the parameters of the double activation energy level was derived without accounting for excited states and valley orbital splitting.

As a result, fitting this equation to the measured temperature-dependence of carrier concentration did not yield meaningful results.

Figures 24, 25, and 26 show the carrier concentration versus T^{-1} for the two undoped Cree substrates (B0436-5B and B0428-2H), and the NASA-grown undoped epilayer (1312-3) respectively. The solid line represents curve-fitting using a variation of equation (26) that takes into account excited states and valley orbital splitting [57].

Table 7 shows the results of this curve-fitting. The activation energies E_h and E_c for the hexagonal and cubic sites found in this table are generally comparable to those in Table 4 obtained from the literature, except for those for the sample B0428-2H. The published range of E_h values is from 0.063 to 0.1 eV and E_c values is from 0.118 to 0.155 eV. As seen in Table 7, the values of E_h and E_c for the n-type sample B0428-2H are considerably lower than the published values, whereas for the n-type samples B0436-5B and 1312-3 they are comparable to the published values. This discrepancy is, to an extent, understandable if it is taken into consideration how difficult it is to do five-parameter curve fitting.

Unlike the results reported by W. Suttrop et al [30], this research did not find $N_h:N_c = 1:2$, where N stands for donors or acceptors and the subscripts h and c stand for hexagonal and cubic sites. In the published literature, the

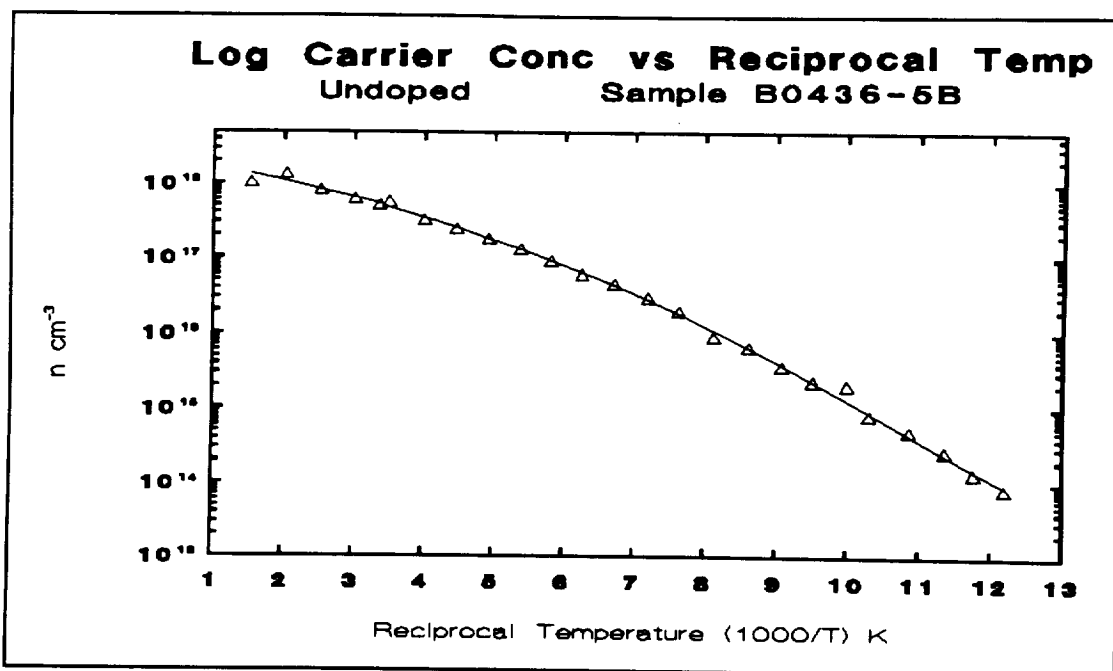


Figure 24 Carrier Concentration as a function of temperature (double level model, sample B0436-5B).

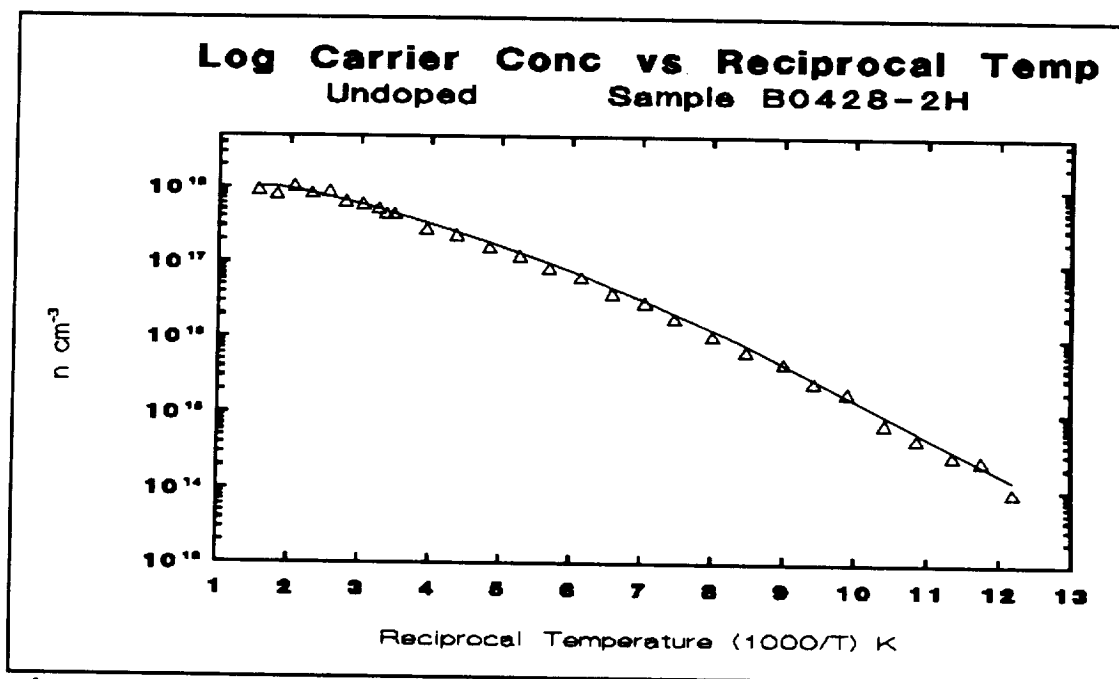


Figure 25 Carrier Concentration as a function of temperature (double level model, sample B0428-2H).

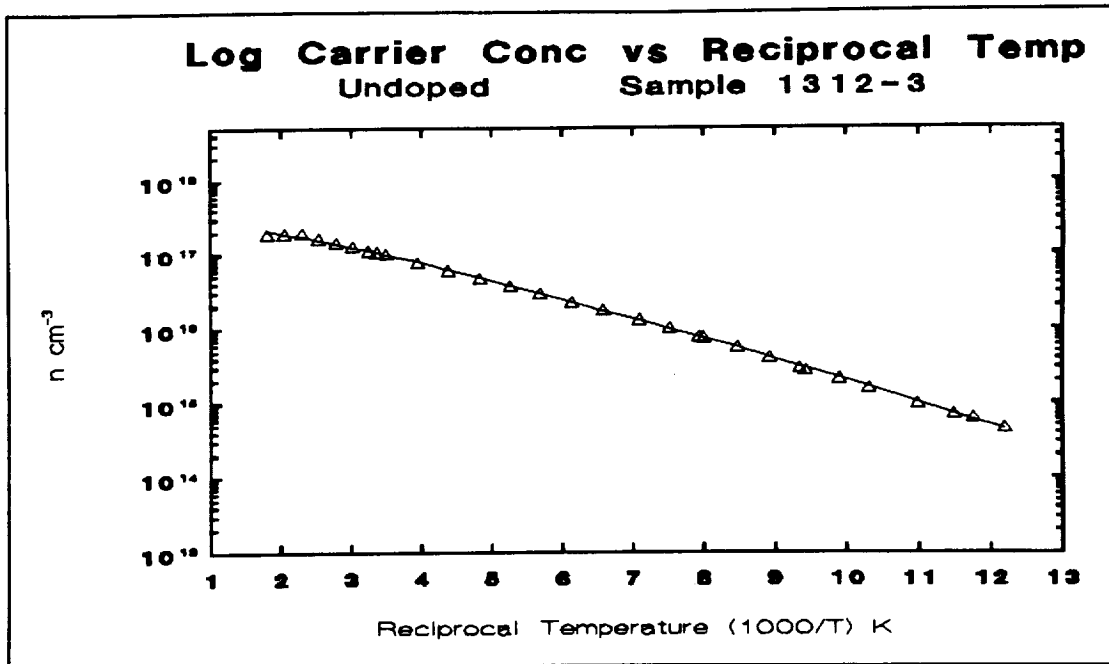


Figure 26 Carrier Concentration as a function of temperature (double level model, sample 1312-3).

Table 7 Calculated Activation Energy and Impurity Concentrations from the Double Level Model.

Sample	Activation Energy		Dopant Concentration		
	E_{dh} eV	E_{dc} eV	N_h cm^{-3}	N_c cm^{-3}	N_{comp} cm^{-3}
B0436-5B n-type	0.093	0.126	1.60e18	5.42e18	3.65e16
B0428-2H n-type	0.010	0.085	6.66e17	1.61e18	5.60e17
1312-3 n-type	0.056	0.113	3.33e17	4.18e17	2.03e17

ratio N_c/N_h is found to vary between 1.4 and 77, with the majority of values of this ratio within 2 ± 0.5 . This research found this ratio to be 3.4 for the sample B0436-5B and 1.25 for the sample 1312-3.

From the published values of E_h and E_c for nitrogen in 6H-SiC, the difference $E_c - E_h$ ranges from 30 meV to 57 meV. This research found this energy difference to be 33 and 57 meV for the samples B0436-5B and 1312-3 respectively.

It was not possible to fit the double level model to the temperature-dependent carrier concentration data of the p-type sample 1270-2 due to the limited reliable data. Most researchers do not find a double level result using electrical characterization for p-type material.

5.2.4 Results of $\mu_n(T)$

The mobility data is presented in Figure 27. The top three curves are for undoped (n-type) samples and the bottom curve is for the p-type sample. All four samples show a decrease in mobility as the temperature is increased. For the undoped samples, the room temperature mobility (also given in Table 5) of electrons decreases with increasing total ($N_d + N_a$) impurity concentration found from single level analysis. The room temperature hole mobility for $\sim 10^{18}/\text{cm}^3$ p-doped sample is about 1/3 of the room temperature electron mobility for comparably n-doped samples.

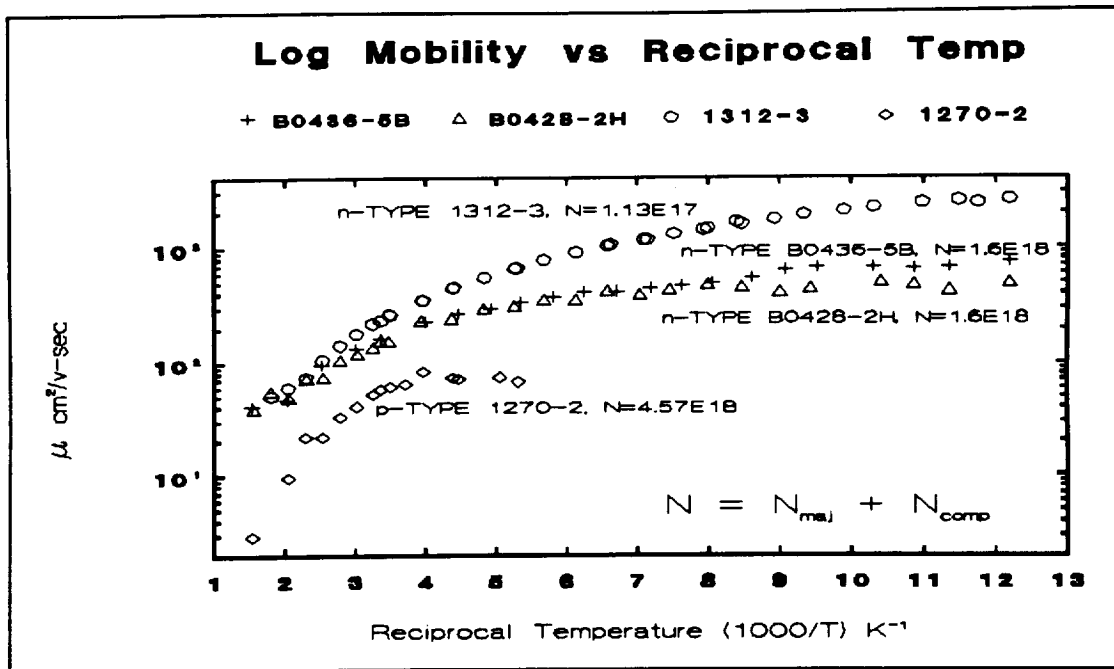


Figure 27 Mobility as a function of temperature for the four test samples.

5.3 Summary

Both the single and double activation energy level models have been used in this research to characterize 6H-SiC substrates and epilayers by fitting the models with the temperature dependent carrier concentration. The activation energies found from both these models are, in general, in fair agreement with those found in the literature.

5.4 Recommendations for Future Work

- A. More research is needed to firmly establish the double activation energy model in terms of 1) finding the accurate values of the cubic and hexagonal activation energy levels, 2) finding the dopant concentration for each activation energy level and finding the dopant dependence of the activation energies, for both p- and n-type SiC.
- B. The accuracy and efficiency of the measurements can be further improved by doing the following:
 - 1.) using an automated Hall rig for data acquisition,
 - 2.) using photolithographically mesa etched epilayers for accurately defining the sample geometry,
 - 3.) using ultrasonically wire-bonded contacts,
 - 4.) using non-magnetic thermocouples, and
 - 5.) using a magnetic power supply that allows reversing the direction of the magnetic field.

BIBLIOGRAPHY

1. Günther Ziegler, Peter Lanig, Dietmar Theis, Claus Weyrich, IEEE Transactions on Electron Devices, Volume ED-30 (4), p. 277 (1983).
2. Robert W. Keyes, Proceedings of the Third International Conference on SiC, p. 534 (1973).
3. S.M. Sze, Physics of Semiconductor Devices (2nd), John Wiley & Sons Inc., p. 850 (1981).
4. Glen A. Slack, Journal of Applied Physics, Volume 35 (12), p. 3460 (1964).
5. H.S. Berman, T.M. Heng, H.C. Nathenson, R.B. Campbell, Third International Conference on SiC, p. 500 (1973).
6. W.v. Muench, E. Pettenpaul, Journal of Applied Physics, Vol. 48 (11), p. 4823 (1977).
7. P.A. Glasow, Springer Proceedings in Physics, Vol. 34, p. 13 (1989).
8. H.J.v. Daal, E.F. Knippenberg, J.D. Wasscher, Journal of Physics of Chemical Solids, Volume 24, p. 109 (1963).
9. H.J.v. Daal, Phillips Research Reports Supplements, Vol. 3, p. 70 (1965).
10. Yu.M. Tairov, V.F. Tsvetkov, Journal of Crystal Growth, Volume 52, p. 146 (1981).
11. Lyle Patrick, Physics Review, Vol. 127 (6), p. 1878 (1962).
12. H.J.v. Daal, C.A.A.J. Greebe, W.F. Knippenburg, H.J. Vink, Journal of Applied Physics, Supplement to Volume 32(10), p. 2225 (1961).
13. S. Karmann, W.Suttrop, A. Schöner, M. Schadt, C. Haberstroh, F. Engelbrecht, R. Helbig, G. Pensl, R.A. Stein, and S. Leibenzeder, Journal of Applied Physics, Vol. 72(11), p. 5437 (1992).
14. W.J. Schaffer, H.S. Hong, G.H. Negley, and J.W. Palmour, Inst. Phys. Conf., Fifth SiC and Related Materials Conference, No. 137 Chapter 3, p. 155 (1994).

15. G.A. Lomakina, Yu. A. Vodakov, E.N. Mokhov, V.G. Oding, G.F. Kholuyanov, Soviet Physics-Solid State, Vol. 12 (10), p. 2356 (1971).
16. S.H. Hagen, C.J. Kapteyns, Phillips Research Reports, Vol. 25 (1), p. 1 (1970).
17. Gerhard Pensl, Reinhard Helbig, Hong Zhang, Gonther Ziegler, Peter Lanig, Materials Research Society Symposium Proceedings, Vol. 97, p. 195 (1987).
18. T. Tachibana, H.S. Kong, Y.C. Wang, R.F. Davis, Journal of Applied Physics, Vol. 67 (10), p. 6375 (1990).
19. H.H. Woodbury, G.W. Ludwig, Physics Review, Vol. 124 (4), p. 1083 (1961).
20. G.N. Violina, Yeh Liang-hseu, G.F. Kholuyanov, Soviet Physics-Solid State, Vol. 5 (12), p. 2500 (1964).
21. O.V. Vakulenko, O.A. Guseva, Soviet Physics Semiconductors, Vol. 15 (8), p. 886 (1981).
22. G.A. Lomalina, Third International Conference on SiC, p. 520 (1973).
23. M. Ikeda, H. Matsunami, T. Tanaka, Physics Review B, Vol. 22 (6), p. 2842 (1980).
24. O.V. Vakulenko, Soviet Physics-Solid State, Vol. 15 (9), p. 1904 (1974).
25. W. Suttrop, G. Pensl, P. Lanig, Applied Physics A, Vol. 51, p. 231 (1990).
26. M.M. Anikin, A.A. Lebedev, A.L. Syrkin, A.V. Suvorov, Soviet Physics Semiconductors, Vol. 19 (1), p. 69 (1985).
27. R.F. Davis, The Electrochemical Society, Extended Abstracts, Vol. 89 (2), p. 707 (1989).
28. W. Suttrop, G. Pensl, The Electrochemical Society, Extended Abstracts, Vol. 89 (2), p. 716 (1989).
29. W.J. Choyke, L. Patrick, Physics Review, Vol. 127 (6), p. 1868 (1962).

30. W. Suttrop, G. Pensl, W.J. Choyke, R. Stein, and S. Leibenzeder, Journal of Applied Physics, Volume 72 (8), p. 3708 (1992).
31. A.I. Veinger, A.A. Lepneva, G.A. Lomakina, E.N. Mokhov, V. I. Sokolov, Soviet Physics Semiconductors, Vol. 18 (11), p. 1256 (1984).
32. M.V. Alekseenko, A.G. Zabrodskii, M.P. Timofeev, Soviet Physics Semiconductors, Vol. 21 (5), p. 494 (1987).
33. H. Zhang, G. Pensl, The Electrochemical Society, Extended Abstracts, Volume 89 (2), p. 714 (1989).
34. I.I. Parfenova, Yu.M. Tairov, V.F. Tsvetkov, Soviet Physics Semiconductors, Volume 23 (2), p. 158 (1990).
35. Ya. É. Kirson, É.É. Klotyn'sh, R.K. Kruminya, Soviet Physics Semiconductors, Vol. 12 (4), p. 473 (1978).
36. Robert F. Pierret, Modular Series on Solid State Devices, Vol. 6, p. 99 (1989).
37. B. Ellis, T.S. Moss, Proceedings Royal Society A, Vol. 299, p. 383 (1967).
38. B. Ellis, T.S. Moss, Proceedings Royal Society A, Vol. 299, p. 393 (1967).
39. H.G. Junginger, W.v. Haeringen, Physica Status Solidi, Vol. 37, p. 709 (1970).
40. J. Anthony Powell, Materials Research Society Symposium Proceedings, Vol. 97, p. 159 (1987).
41. W.F. Knippenberg, Philips Research Reports, Vol. 18 (3), p. 161 (1963).
42. L.J.v. der Pauw, Philips Research Reports, Vol. 13, p.1 (1958).
43. Edited by H.H. Wieder, Material Science Monographs, Laboratory Notes on Electrical and Galvanomagnetic Measurements, 2, Pub. Elsevier, p. 26 (1979).
44. ASTM Designation F76-86, p. 120-132.
45. David Halliday, Robert Resnick, Physics I & II, John Wiley & Sons Inc., p. 827 (1967).
46. E.H. Putley, The Hall Effect and Related Phenomena, Butterworth & Co. Limited (1960).

47. Daniel W. Koon, Review Scientific Instrumentation, Vol. 60 (2), p. 271 (1989).
48. Dennis G. Peters, John M. Hayes, Gary M. Hieftje, Chemical Separation and Measurements, Theory and Practice of Analytical Chemistry, Saunders Golden Sunburst Series, p. 6 (1971).
49. Mark Lundstrom, Modular Series on Solid State Devices, Volume X, Addison-Wesley Co., (1990).
50. Akira Itoh, Hironobu Akita, Tsunenobu Kimoto, and Hiroyuki Matsunami, Inst. Phys. Conf., Fifth SiC and Related Materials Conference, No. 137 Chapter 1, p. 59 (1994).
51. W.v. Muench, I. Pfaffened, Journal Applied Physics, Vol. 48 (11), p. 4831 (1977).
52. L. Patrick, W.J. Choyke, Physics Review B, Vol. 2 (6), p. 2255 (1970).
53. Phillip R. Bevington, Data Reduction and Error Analysis for the Physical Sciences, McGraw-Hill Book Co., (1969).
54. J.S. Blakemore, Semiconductor Statistics, MacMillian Co., (1962).
55. Stuart Hollingdale, Makers of Mathematics, Penguin Books, (1989).
56. D. Michael Stretchberry, A Summary of the Measurement and Interpretation of the Hall Coefficient and Resistivity of Semiconductors, Lewis Research Center, Cleveland, OH, (NASA TM X-1711)
57. Dr. Edward Haugland, NASA Lewis Research Center, private communication, September 1994.

APPENDIX A

Tables

Table 8 Parameter Values¹ (at room temperature)

Parameters	Si	Ge	GaAs	6H-SiC
Bandgap E_g (eV)	1.12	0.66	1.42	2.93 [50]
Thermal Conductivity κ (W/cm K)	1.5	0.6	0.46	4.9 [4]
Optical-Phonon Energy E_o (eV)	0.063	0.037	0.035	0.1205 [6]
Saturated Drift Velocity v_L (cm/sec)	1×10^7 [5]	6×10^6 [2]	2×10^7 [6]	2×10^7 [6]
Breakdown Field E_B (V/cm)	3×10^5	1×10^5	4×10^5	2×10^7 [51]
Dielectric Constant (Static) ϵ	11.9	16.0	13.1	19.66 [52]

¹ All of the parameter values were taken from reference [3] except SiC and saturated drift velocity values.

Table 9 Calculated Figures of Merit at 300 K

Figure of Merit	Si	Ge	GaAs	SiC
Johnson (V/s) ²	7.16×10^{23}	1×10^{22}	1.9×10^{24}	1.27×10^{26}
Keyes (W/s-°C)	6.7×10^7	5×10^7	2.95×10^7	3.44×10^8

APPENDIX B

History and Nomenclature of SiC

B.1 Introduction

Silicon carbide is an unusual semiconductor which rarely occurs in nature. In the solid state, it is the only known compound of silicon and carbon. Its existence has been known since the 19th century; it has yielded its secrets very slowly, however.

This appendix will give a brief history of the metamorphosis of silicon carbide from something that occurred by chance in single crystal form as a byproduct of the Acheson process of making abrasive, to something that is now produced, doped or undoped, in the form of sublimation grown boules, using the modified Lely method, in continually increasing diameters. Currently, there are enough applications of SiC, so that once the wafer diameter exceeds three inches of usable surface area the material should be a competitive semiconductor.

This appendix will also attempt to explain the nomenclature associated with silicon carbide, i.e. such things as polytype naming. There are in excess of 130 different polytypes of silicon carbide that have been found

thus far; this is a small fraction of those that are theoretically possible.

B.2 History

The hardness of silicon carbide is between diamond and topaz [41] or sapphire [40] and only diamond and boron nitride are harder.

The commercial value of silicon carbide [41] as a cutting and polishing abrasive was realized by A.H. and E.H. Cowless who had a U.S. patent for the production of silicon carbide in 1885 and A.G. Acheson who had a British patent in 1892.

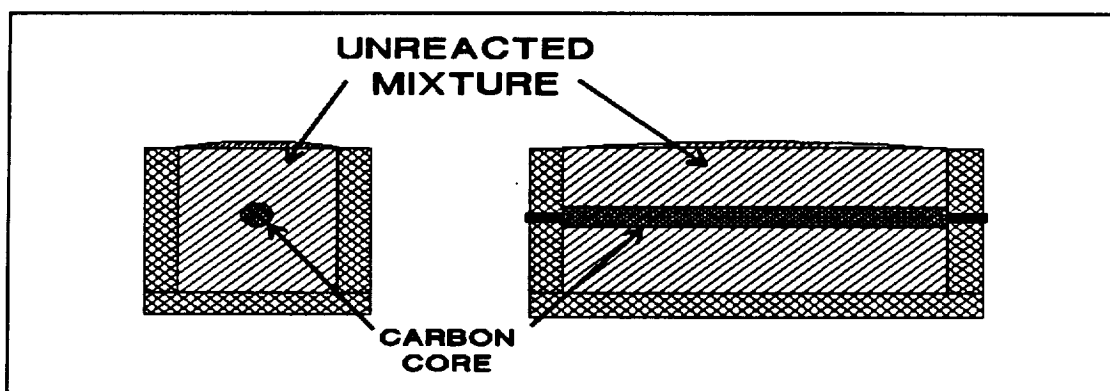


Figure 28 Acheson Furnace

The Acheson process involves filling a rectangular volume, as seen in Figure 28, with the reactants: sand 50%, coke 40%, sawdust 7%, and NaCl 3%. Through the center of this mixture runs a carbon core which is the electrical heating element. The time-temperature heating cycle exceeds 30 hours with a maximum temperature of 2700°C.

During this process the sawdust shrivels, keeping the mixture porous. The salt reacts with impurities and the volatile reactants escape with the large volume of carbon monoxide generated, helping to improve the purity of the mixture.

The mixture settles during the heating process forming voids in the SiC mass. The Acheson crystals are found in these voids. These crystals usually have an area of a few cm² with a thickness of a few mm. They usually have one well developed face. These crystals are heavily doped with a mixture of dopants and polytypes. The reaction results in predominantly one polytype, 6H. There are a large number of imperfections, e.g. twinning, and screw dislocations, in the crystal structure as well.

These crystals were all that were available to the scientific community until 1955 when J.A. Lely published his method of growing purer crystals of known doping.

The Lely method emulates the sublimation and recrystallization that occurs in the voids formed during the Acheson process on a laboratory scale. In later runs of the Lely method, a porous graphite cylinder is surrounded with the purest, light green, technical grade polycrystalline silicon carbide available (Fig. 29). The charge of polycrystalline SiC in the Lely chamber is heated to 2500°C. in an argon atmosphere to which dopants can be added, i.e. dopants can be introduced by adding them to either the

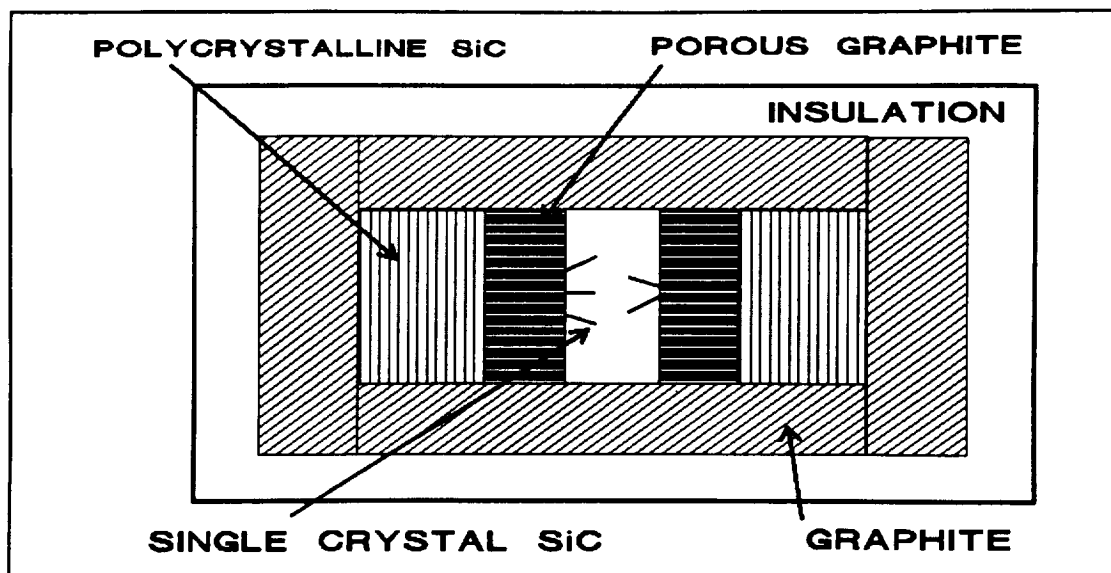


Figure 29 Lely Chamber

polycrystalline silicon carbide or to the argon. The SiC diffuses through the graphite cylinder and recrystallizes as single crystals on the interior of the porous cylinder.

In practice, the yield is very low and the nucleation is uncontrolled. This was a tremendous improvement over the Acheson process in spite of its drawbacks. The yield was predominantly of the 6H polytype followed by the 15R and the 4H polytypes [15,40].

The publication of two papers [1,10] using a seed crystal solved the nucleation problem of the Lely method. The resulting single crystal grows both in thickness and in width from the seed crystal. The modified Lely method (Figure 30) uses a porous graphite cylinder with the seed at the cooler part of the temperature gradient 2200 to 2300 [7] or 2400°C [1].

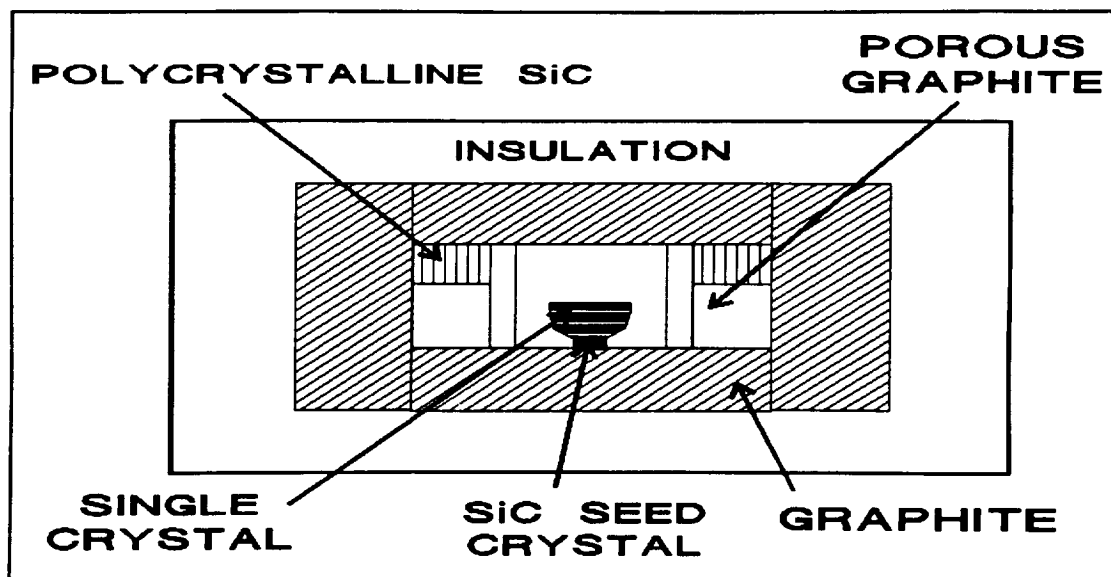


Figure 30 Modified Lely Chamber

The starting material is the purest SiC available or it could be compounds that contain either silicon or carbon or both. Doping is accomplished through the dopants in the starting material or by adding them to the atmosphere in the growth chamber. The three essential parameters are the temperature which determines the polytype, the temperature gradient and the pressure which determine the transport velocity, i.e. the growth velocity. High pressure is used to retard the growth until the proper temperature has been reached.

The grown boules are cut into slices with a diamond wafering saw and the exterior, of polycrystalline material that forms during cool down, is removed by coring the center of the slice. The wafers are then polished. SiC can be visualized as stacked layers, and the layers are double layers with a close packed layer of silicon and a layer of

carbon. Each of the carbon atoms is directly above each of the silicon atoms. Therefore, each wafer always has a carbon face and a silicon face.

B.3 Structure and Nomenclature

Silicon and carbon are both group four elements making SiC a IV-IV compound semiconductor. Each silicon atom is tetrahedrally surrounded by four carbon atoms and each carbon atom is likewise surrounded tetrahedrally by four silicon atoms. The atoms form parallel planes visualized as mentioned in the previous section, as double layers of silicon and carbon atoms when viewed along the $11\bar{2}0$ plane [40,41].

If a plane of close packed spheres is viewed from above (or below) there are six spaces around each sphere and two ways to stack another plane of close packed spheres on the first plane; the second plane will occupy three of the six spaces. Using an A, B, C position notation, the first plane is the A position, the second plane is in the B position and the third can be in either the A or the C position (Fig. 31). Each additional plane can occupy one of the two positions not already occupied by the underlying plane, possibly forming large unit cells. The layers can form either cubic (trigonal) or hexagonal symmetry. As an example in cubic symmetry the adjacent layers of B are in

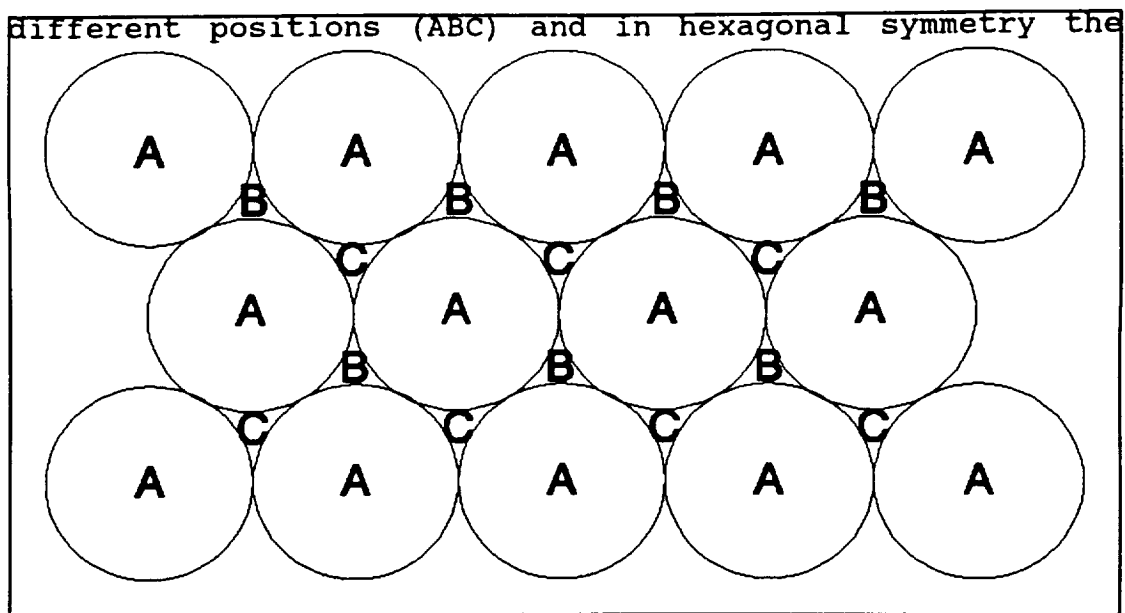


Figure 31 Close Packed Spheres

adjacent layers of B are in the same position (ABA).

The polytypes form either cubic (C), also called beta-SiC, hexagonal (H), or rhombohedral (R) structures; the latter two are also referred to as alpha-SiC.

There are several different notations used to identify the crystal structure. The Ramsdell notation uses a number followed by a letter. The number represents the number of double layers in the unit cell and the letter represents the structure, e.g. cubic (C), hexagonal (H), or rhombohedral (R). The Jagodzinski notation characterizes the layers by adjacent layers in the unit cell. That is whether they are cubic or hexagonal.

Table 10 gives some examples of different polytypes (3C,6H) in different notations and the number of inequivalent sites.

Table 10 Polytype Notation

RAMSDELL	STACKING	JAGODZINSKI	INEQ	H E X	C U B
2H	AB	h(h)	1	1	0
3C	ABC	c(c)	1	0	1
4H	ABAC	hc(c)	2	1	1
6H	ABCACB	hcc(hcc)	3	1	2
15R	ABCACACBCABACBCB	hcchc(hcchc)	5	2	3

The bandgap extremes are 2.2 eV for 3C and 3.2 eV for 2H. The bandgap is approximately inversely proportional to the fraction of each inequivalent site type. As an example, the 6H polytype has 1/3 of its inequivalent sites of the hexagonal type and 2/3 of its inequivalent sites of the cubic type, so $1/3$ of 3.2 + $2/3$ of 2.2 = 2.867. The bandgap of 6H is reported to be 2.93 eV.

APPENDIX C

Least Squares

C.1 Introduction

Designing and conducting an experiment to obtain the best possible data requires a significant investment of time and effort. The data then needs to be evaluated to extract results that are unique, unambiguous, and with the smallest possible error. The least squares approach yields values that are normally distributed about the true values with the smallest variance. This appendix will briefly explain the least squares method of analysis and how it was applied in this study.

C.2 Least Squares Method

Least squares is a method of analysis, developed by Carl Friedrich Gauss in the 18th century (c.1795), where a set of parameters (P_j) are estimated from measurements of some other related quantities (Y_i) so that the difference between the experimental (or observed) values and the

adjusted (or calculated) values are minimized. Theoretically the adjusted values are closer to the true values than the observed values.

The basis for the least squares method is that the errors between the observed data values and the calculated values can be described by the normal (Gaussian) error distribution function. When this is true the likelihood function takes the following form:

$$l(P) = \text{constant} - S / (2\sigma^2) \quad (54)$$

where $l(P)$ is the likelihood that the parameter P is the correct value, σ^2 is the variance of the data and S is the sum of squares function given by

$$S = \sum_{i=1}^n (Y_i - Y(X_i, P_1, P_2, \dots, P_j))^2 \quad (55)$$

In the sum of squares function Y_i is the observed value and the function $Y(X_i, P_1, P_2, \dots, P_j)$ is the calculated or adjusted value based on an appropriate modeling equation.

Then the maximum likelihood function $[dl(P)/dP]$ reduces to the method of least squares. This is the reason the weighting factor, the reciprocal of the variance, needs to be included in every calculation.

The weighted sum of squares S is the fundamental equation of the least squares method.

$$S = \sum_{i=1}^n \left(\frac{1}{\sigma_i^2} [Y_i - Y(X_i, P_1, P_2 \dots P_j)]^2 \right) \quad (56)$$

The object is to make S as small as possible. When S is minimized, by definition, the derivatives of S are all equal to zero. Then by taking the partial derivatives of S with respect to each parameter $(\partial S / \partial P_j)$, a set of equations is produced which can be used to solve for the parameters of interest.

C.3 Least Squares Applied

This study follows the procedures outlined by Philip R. Bevington for the linearization of the fitting function in reference [53] to evaluate the data. He uses the gradient-expansion algorithm of Marquardt to combine the best features of the gradient search with the method of linearizing the fitting function. This is necessary since the gradient search is best when approaching the minimum from a distance, but converges slowly when near the minimum; and the analytical method of using a Taylor's expansion of the fitting function $y(x)$ can only be used reliably when in the immediate vicinity of the minimum. The algorithm offers the advantage that only the simpler first-order expansion needs to be valid when near the minimum.

The algorithm increases the diagonal terms of the curvature matrix α which he defines as

$$\alpha_{jk} = \sum_i \left[\frac{1}{\sigma_i^2} \frac{\partial Y(X_i)}{\partial P_j} \frac{\partial Y(X_i)}{\partial P_k} \right] \quad (57)$$

by a factor λ which determines which method predominates during an iteration. If λ is very small, the solution is similar to a Taylor's expansion like the analytical method. If λ is very large, the diagonal terms dominate giving n separate equations and the solution is similar to the gradient search method.

Marquardt's recipe as given in ref. [53] is the following:

1. Compute $S(P)$.
2. Start initially with $\lambda = 0.001$.
3. Compute δP and $S(P+\delta P)$ with this choice of λ .
4. If $S(P+\delta P) > S(P)$, increase λ by a factor of 10 and repeat step (3).
5. If $S(P+\delta P) < S(P)$, decrease λ by a factor of 10, consider $P' = P+\delta P$ to be the new starting point, and return to step (3) substituting P' for P .

This is done so that S decreases and λ is small enough to make use of the analytical method. This algorithm was

implemented by the computer subroutine CURFIT which was modified to make it run more efficiently and without overflows¹⁶.

¹⁶ The modified subroutine CURFIT was made available to me courtesy of Dr. Edward Haugland of NASA LeRC.

```

C SUBROUTINE CURFIT  -- FROM BEVINGTON'S BOOK, PG. 237
C
C PURPOSE
C   MAKE A LEAST-SQUARES FIT TO A NON-LINEAR FUNCTION
C   WITH A LINEARIZATION OF THE FITTING FUNCTION
C
C USAGE
C   CALL CURFIT (X, Y, SIGMAY, NPTS, NTERMS, MODE, A,
C               DELTAA, SIGMAA, FLAMDA, YFIT, CHISQR)
C
C DESCRIPTION OF PARAMETERS
C   X      - ARRAY OF DATA POINTS FOR INDEPENDENT VARIABLE
C   Y      - ARRAY OF DATA POINTS FOR DEPENDENT VARIABLE
C   SIGMAY- ARRAY OF STANDARD DEVIATIONS FOR Y DATA POINTS
C   NPTS   - NUMBER OF PAIRS OF DATA POINTS
C   NTERMS- NUMBER OF PARAMETERS
C   MODE   - DETERMINES THE METHOD OF WEIGHTING THE FIT
C             +1 (INSTRUMENTAL) WEIGHT(I) = 1/SIGMA(I)**2
C             0  (NO WEIGHTING)  WEIGHT(I) = 1
C             -1 (STATISTICAL)  WEIGHT(I) = 1/Y(I)
C   A      - ARRAY OF PARAMETERS
C   DELTAA- ARRAY OF INCREMENTS FOR PARAMETERS A
C   SIGMAA- ARRAY OF STANDARD DEVIATIONS FOR PARAMETERS A
C   FLAMDA- PROPORTION OF GRADIENT SEARCH INCLUDED
C   YFIT   - ARRAY OF CALCULATED VALUES OF Y
C   CHISQR- REDUCED CHI SQUARE FOR FIT
C
C SUBROUTINES AND FUNCTION SUBPROGRAMS REQUIRED
C   FUNCTN (X,I,A)
C     EVALUATES THE FITTING FUNCTION FOR THE ITH TERM
C   FCHISQ (Y,SIGMAY,NPTS,NFREE,MODE,YFIT)
C     EVALUATES REDUCED CHI SQUARE FOR FIT TO DATA
C   FDERIV (X,I,A,DELTAA,NTERMS,DERIV)
C     EVALUATES THE DERIVATIVES OF THE FITTING FUNCTION
C     FOR THE ITH TERM WITH RESPECT TO EACH PARAMETER
C   MATINV (ARRAY,NTERMS,DET)
C     INVERTS A SYMMETRIC TWO-DIMENSIONAL MATRIX OF DEGREE
C     NTERMS AND CALCULATES ITS DETERMINANT
C
C COMMENTS
C   DIMENSION STATEMENT VALID FOR NTERMS UP TO 10
C   SET FLAMDA = 0.001 AT BEGINNING OF SEARCH
C   CALCULATED VALUES OF SIGMAA(J) DEPEND ON VALUE OF FLAMDA
C   SET FLAMDA = 0.0 AFTER CONVERGENCE TO CALCULATE SIGMAA(J)
C
C CHANGES FROM BEVINGTON ORIGINAL
C   CHANGED STMTS 73 AND 84 SLIGHTLY TO PREVENT OVERFLOWS
C   (10/87)

```

```

C   ADDED POSSIBILTIY OF ENTERING FLAMDA = 0. (2/88)
C   ADDED STMT 28 TO ALLOW CALC OF WEIGHT(I) WHEN
C       SIGMAY(I)=0. (3/90)
C   INCREASED DIMENSION OF WEIGHT FROM 100 TO 300 (3/90)
C   ADDED PROVISION FOR ALPHA(J,K)=0. IN DO 73 LOOP (3/90)
C   ADDED PROVISION FOR TYPING VALUES OF ALL MATRIX VALUES

```

```

C
C           EDITED  3/20/90
C

```

```

C   SUBROUTINE CURFIT (X,Y,SIGMAY,NPTS,NTERMS,MODE,A,DELTA,A,
1       SIGMAA,FLAMDA,YFIT,CHISQR)
C   DOUBLE PRECISION ARRAY
C   DIMENSION X(1),Y(1),SIGMAY(1),A(1),DELTA(1),SIGMAA(1),
1       YFIT(1)
C   DIMENSION WEIGHT(300),ALPHA(10,10),BETA(10),DERIV(10),
1       ARRAY(10,10),B(10)
11      NFREE=NPTS-NTERMS
12      IF (NFREE) 13,13,20
13      CHISQR=0.
14      GO TO 110
C
C   EVALUATE WEIGHTS
C
20      DO 30 II=1,NPTS
15      I=II
21      IF (MODE) 22,27,29
22      IF (Y(I)) 25,27,23
23      WEIGHT(I)=1./Y(I)
16      GO TO 30
25      WEIGHT(I)=1./(-Y(I))
17      GO TO 30
27      WEIGHT(I)=1.
18      GO TO 30
28      IF (SIGMAY(I)) 29,27,29
29      WEIGHT(I)=1./SIGMAY(I)**2
30      CONTINUE
C
C   EVALUATE ALPHA AND BETA MATRICES
C
31      DO 34 J=1,NTERMS
19      BETA(J)=0.
20      DO 34 K=1,J
34      ALPHA(J,K)=0.
41      DO 50 II=1,NPTS
21      I=II
22      CALL FDERIV(X,I,A,DELTA,A,NTERMS,DERIV)
23      DO 46 J=1,NTERMS
24      BETA(J)=BETA(J)+WEIGHT(I)*(Y(I)-FUNCTN(X,I,A))*DERIV(J)

```

```

DO 46 K=1,J
ALPHA (J,K)=ALPHA (J,K)+WEIGHT (I)*DERIV (J)*DERIV (K)
46      CONTINUE
50      CONTINUE
51      DO 53 J=1,NTERMS
DO 53 K=1,J
53      ALPHA (K,J)=ALPHA (J,K)
C
C TYPE OUT ALPHA MATRIX (IF DESIRED)
C (FORMAT FOR NTERMS UP TO 7)
C
C TYPE 550
C DO 56 J=1,NTERMS
C56     TYPE 560, (ALPHA (J,K),K=1,NTERMS)
C TYPE 550
C550    FORMAT (/)
C560    FORMAT (5X,1PE11.3,6E11.3)
C
C EVALUATE CHI SQUARE AT STARTING POINT
C
61      DO 62 II=1,NPTS
I=II
62      YFIT (I)=FUNCTN (X,I,A)
63      CHISQ1=FCCHISQ (Y,SIGMAY,NPTS,NFREE,MODE,YFIT)
C
C EVALUATE MODIFIED CURVATURE MATRIX ARRAY
C
71      DO 74 J=1,NTERMS
DO 73 K=1,NTERMS
AX=SQRT (ALPHA (J,J))*SQRT (ALPHA (K,K))
IF (AX) 70,70,72
70      ARRAY (J,K)=0.
LOOP=73
TYPE 200,J,J,K,K,LOOP
GOTO 73
72      ARRAY (J,K)=ALPHA (J,K)/AX
73      CONTINUE
74      ARRAY (J,J)=1.+FLAMDA
C
C TYPE MODIFIED CURVATURE MATRIX, IF DESIRED
C
C TYPE 550
C DO 76 J=1,NTERMS
C76     TYPE 560, (ARRAY (J,K),K=1,NTERMS)
C
C INVERT MODIFIED CURVATURE (ERROR)
C MATRIX TO FIND NEW PARAMETERS
C

```

```

80      CALL MATINV (ARRAY, NTERMS, DET)
C
C TYPE MODIFIED CURVATURE MATRIX, IF DESIRED
C
C TYPE 550
C DO 86 J=1, NTERMS
C86     TYPE 560, (ARRAY (J, K), K=1, NTERMS)
C
81     DO 84 J=1, NTERMS
      B (J) = A (J)
      DO 84 K=1, NTERMS
      AX = SQRT (ALPHA (J, J)) * SQRT (ALPHA (K, K))
      IF (AX) 82, 82, 83
82     LOOP = 84
      TYPE 200, J, J, K, K, LOOP
      GOTO 84
83     B (J) = B (J) + BETA (K) * ARRAY (J, K) / AX
84     CONTINUE
C
C IF CHI SQUARE INCREASED, INCREASE FLAMDA AND TRY AGAIN
C
91     DO 92 II=1, NPTS
      I = II
92     YF IT (I) = F UNCTN (X, I, B)
93     CHISQR = F CHISQ (Y, SIGMAY, NPTS, NFREE, MODE, YF IT)
      IF (FLAMDA) 94, 101, 94
94     IF (CHISQ1 - CHISQR) 95, 101, 101
95     FLAMDA = 10. * FLAMDA
      GO TO 71
C
C EVALUATE PARAMETERS AND UNCERTAINTIES USING ERROR MATRIX
C
101    DO 103 J=1, NTERMS
      LOOP = 103
      A (J) = B (J)
      IF (ARRAY (J, J).LE.0.) TYPE 201, J, J, ARRAY (J, J), LOOP
      IF (ALPHA (J, J).LE.0.) TYPE 202, J, J, ALPHA (J, J), LOOP
      IF (ALPHA (J, J).EQ.0.) ALPHA (J, J) = .1
103    SIGMAA (J) = SQRT (ABS (ARRAY (J, J)) / ABS (ALPHA (J, J)))
      IF (FLAMDA) 104, 110, 104
104    FLAMDA = FLAMDA / 10.
110    RETURN
200    FORMAT (T2 'ALPHA (' I1, I1 ') OR ALPHA (' I1, I1 ') IS
ZERO! DO LOOP', I4)
201    FORMAT (T2 'ARRAY (' I1, I1 ') =', 1PE10.3, ' DO LOOP', I4)
202    FORMAT (T2 'ALPHA (' I1, I1 ') =', 1PE10.3, ' DO LOOP', I4)
      END

```

APPENDIX D

Cryostat Schematics

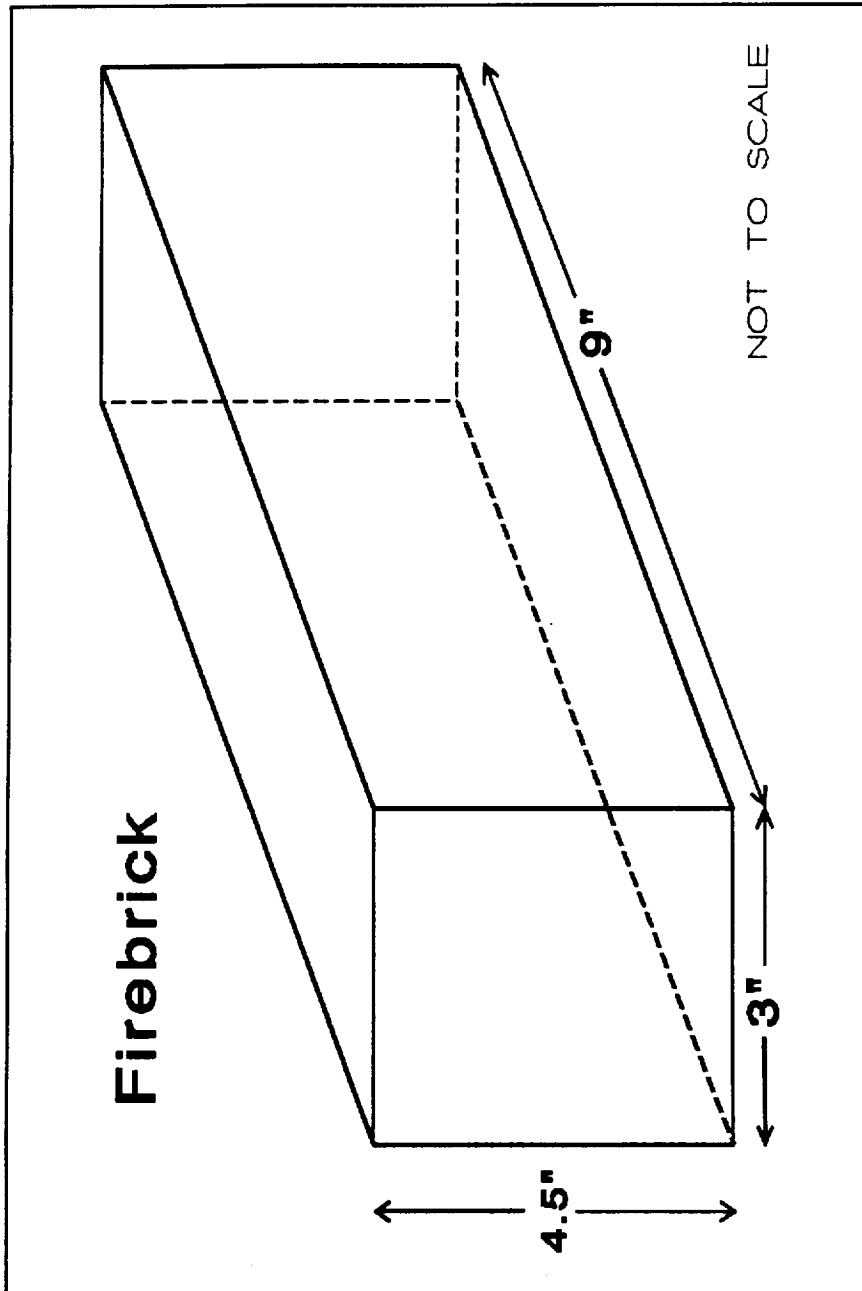


Figure 32 High temperature furnace and sample holder.

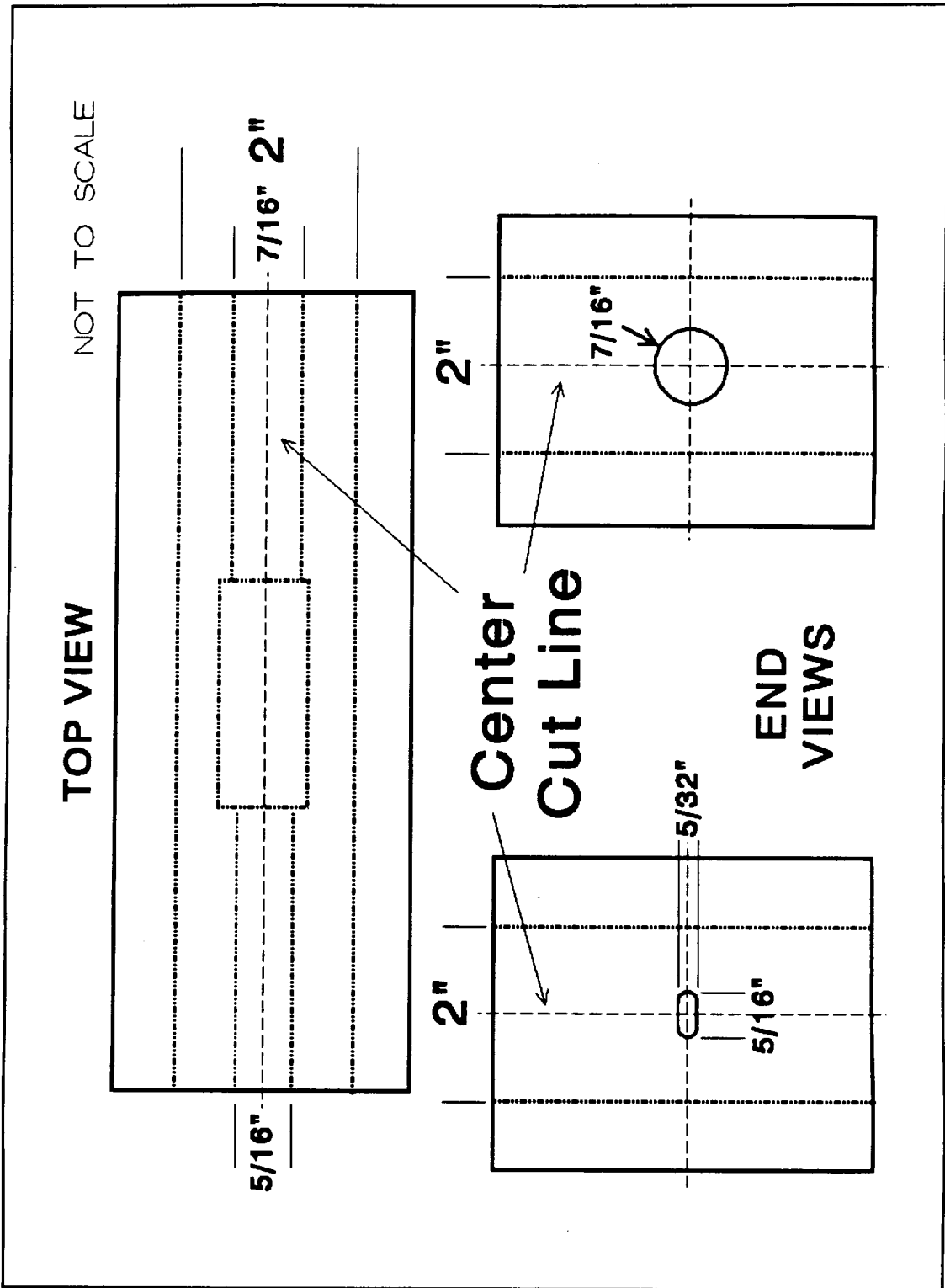


Figure 33 Firebrick machining dimensions.

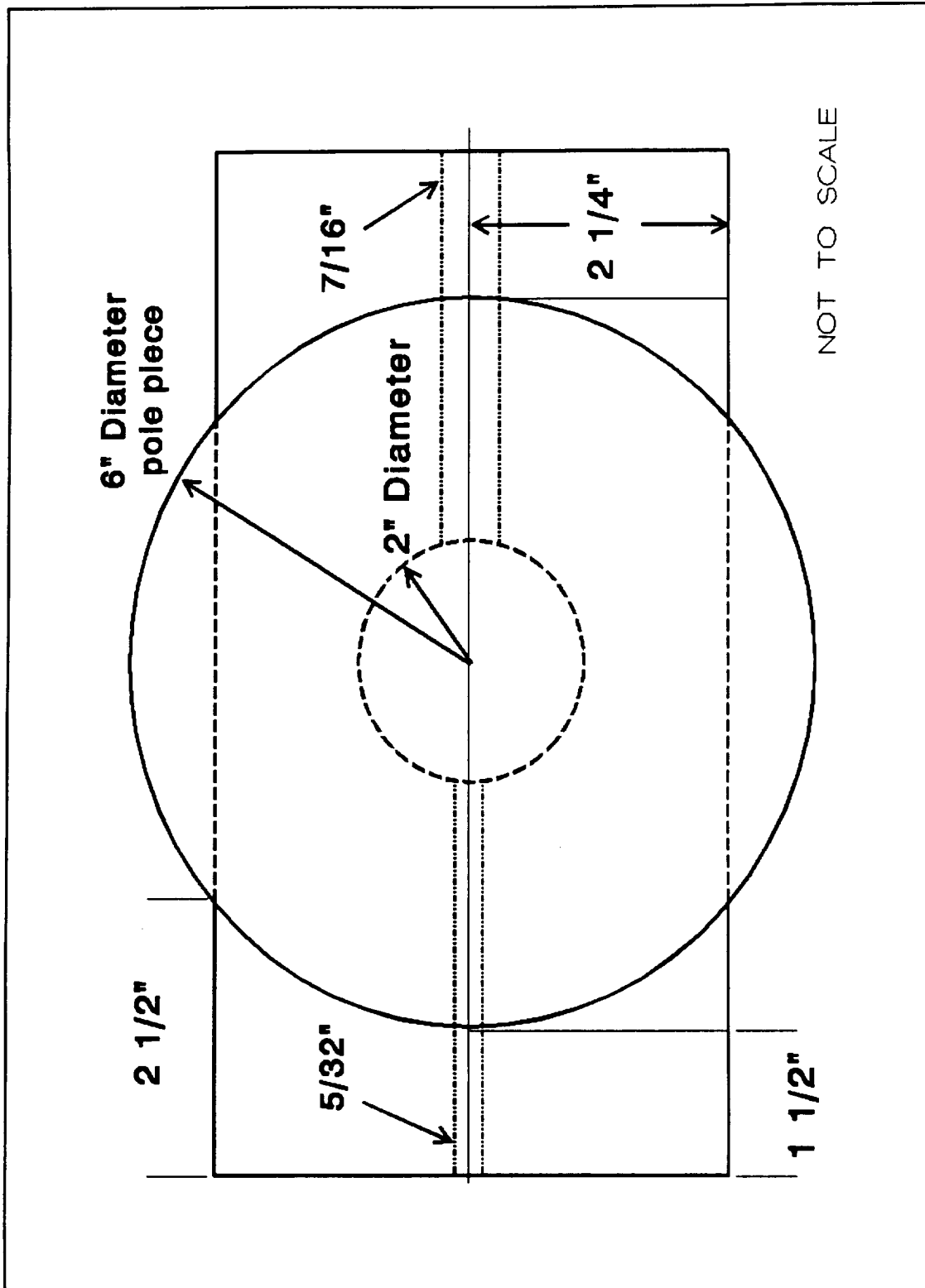


Figure 34 The machined firebrick and magnet's pole piece.

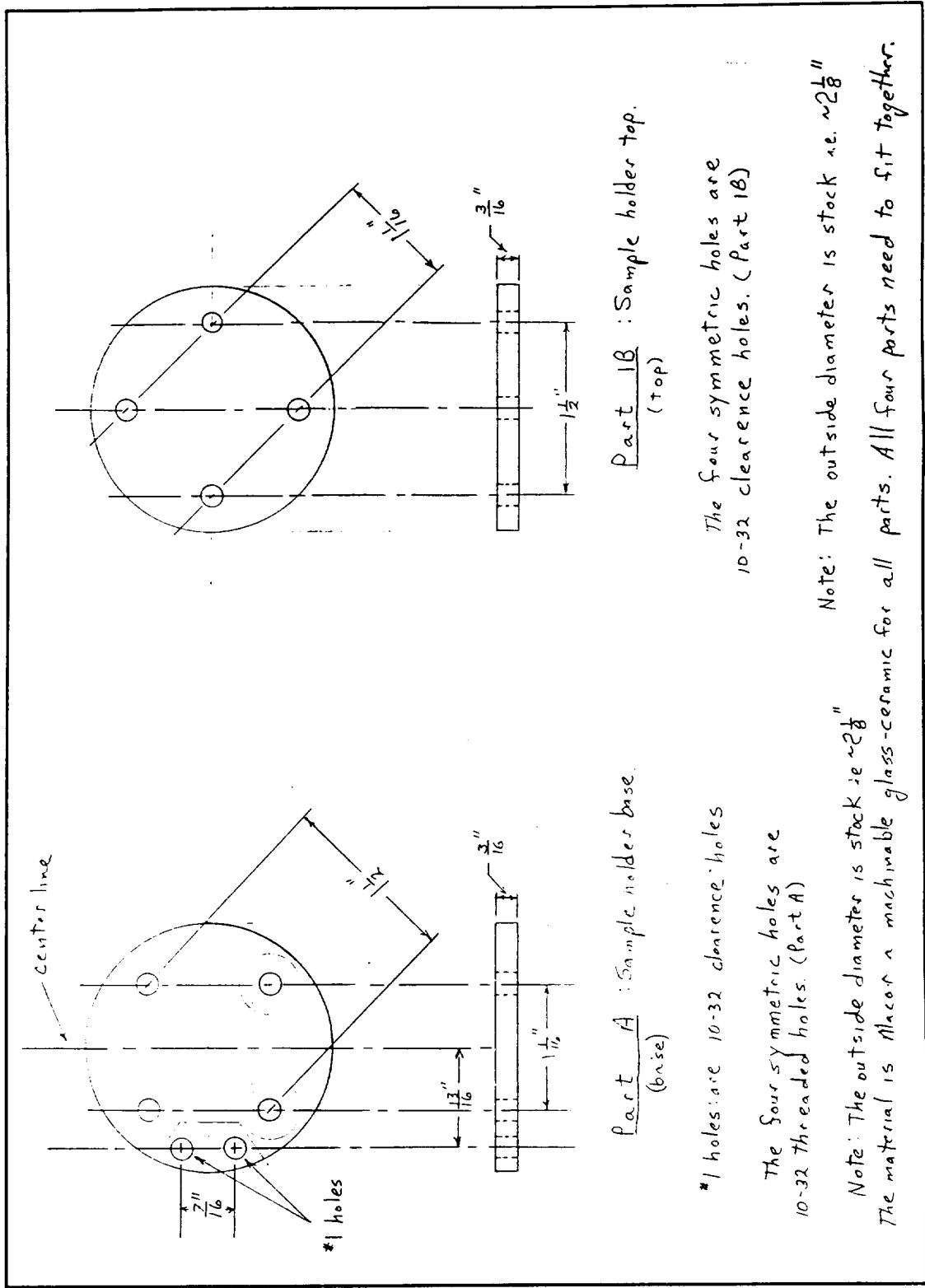


Figure 35 Bottom of the sample platform.

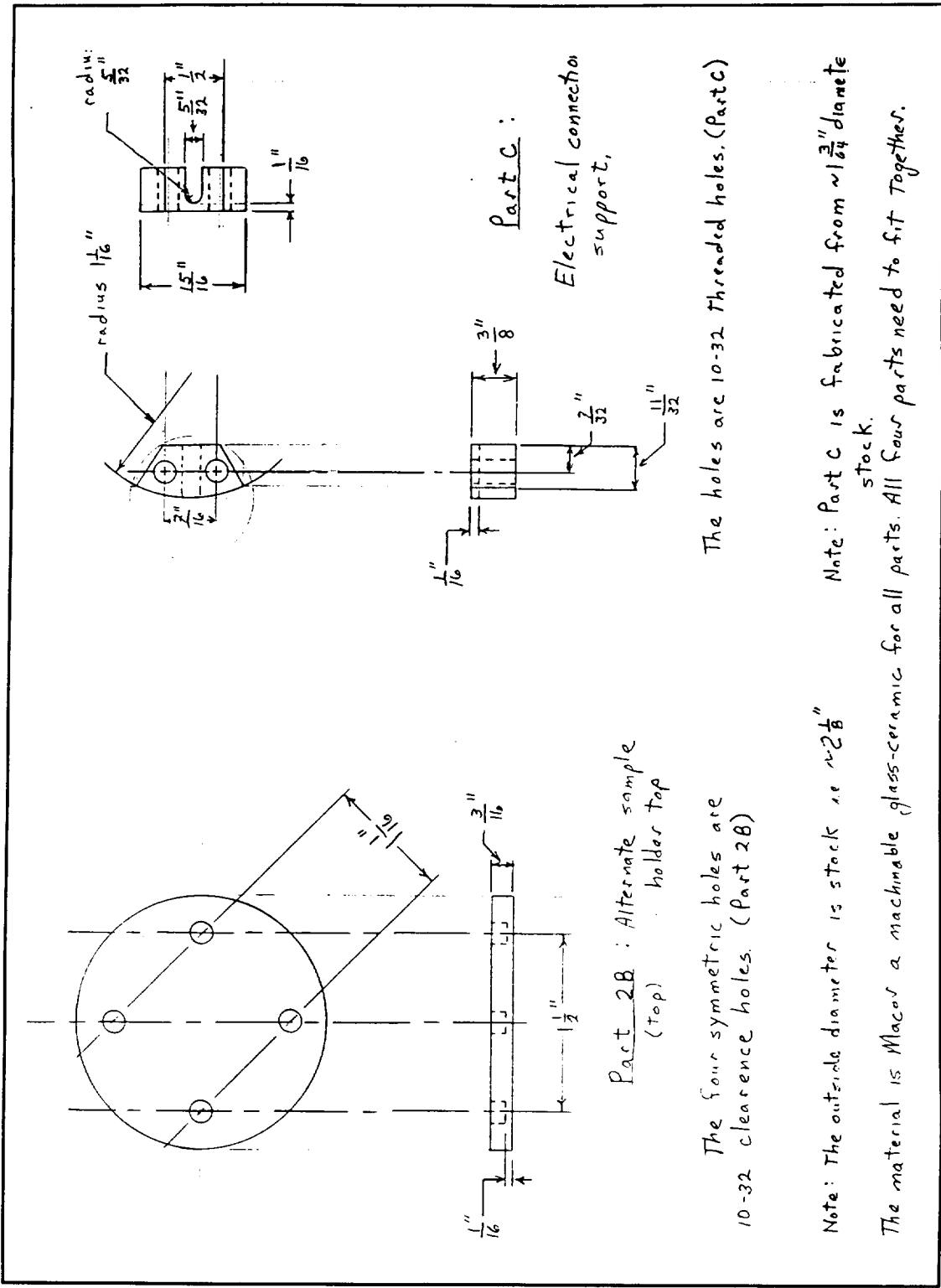


Figure 36 Top of the sample platform and thermocouple support.

APPENDIX E

Effective Mass

The density of states function is used to calculate the carrier concentrations in the material. To do this the density of states effective mass needs to be known.

There are two ways of reporting the effective mass in the literature. One group [6,18,20,21,34] reports results that are consistent with

$$\frac{m^*}{m_0} = (m_l * m_t^2)^{1/3} \quad (58)$$

where m_l is the longitudinal effective mass, m_t is the transverse effective mass, m^* is the effective mass of electrons or holes per conduction band minimum or valence band maximum, respectively. The other group [7,30,32,33,35] reports results that are consistent with [36],

$$\frac{m_d^*}{m_0} = M^{2/3} [m_l * m_t^2]^{1/3} \quad (59)$$

where M is the number of conduction band minima or valence band maximum for electrons or holes, respectively, and m_d^* gives the total density of states effective mass for electrons or holes.

These are used in the calculation of the effective density of states function $N_{c,v}$ given by

$$N_{c,v} = 2M \left[\frac{2\pi m^* kT}{h^2} \right]^{3/2} \quad (60)$$

Here M is included if equation (58) is used and dropped if equation (59) is used for the effective mass, k is Boltzmann's constant, T is the temperature in kelvins, and h is Planck's constant. The subscripts c or v stand for the conduction or valence band respectively.

H. J. van Daal [8] also made a plot, effectively, of

$$\left(\frac{M * m_{dh}^*}{g m_o} \right) \quad (61)$$

versus the reciprocal distance between minority centers. Here, M is the number of valleys in the valence band, m_{dh}^* is the density of states effective mass of holes, and g is the degeneracy factor. For aluminum, he found $(M * m_d^*/g) = 0.5$ which, for $M=1$, $m_d^*=1$, would give $g=2$. He, also, found the effective mass of electrons to range from $0.72m_o$ to $1.0m_o$.

In conjunction with this, there is a controversy in the SiC community concerning the number of conduction band minima that are within the first Brillouin zone. There appear to be six conduction band minima in SiC, just as there are in silicon, but are there 3 or 6 valleys within the first Brillouin zone [20,30,35]? As an example,

germanium [36] has eight conduction band minima but only four are within the first Brillouin zone. Therefore, four is used for M in the effective mass or density of states equation for germanium.

The uncertainties in the number of conduction band minima being 3 or 6, and in the magnitudes of the transverse $(0.24 \text{ to } 0.35)m_0$ and longitudinal $(0.34 \text{ to } 1.5)m_0$ effective masses [21,22,30,35,37,38], could be unsettling. But fortunately, when the total density of states effective mass is calculated using these diverse quantities there is agreement that $m_{de}^* = (1.0 \pm 0.2)m_0$ for electrons in the conduction band; either directly by the reported normalized effective mass [7,9,30,32,33,35] or by calculating m_{de}^* using equation (59) and a three valley approach using the reported per valley effective mass [6,18,20,21,34]. In this research $m_e^* = 0.44 m_0$ was used after Muench et al [6]. Therefore $m_{de}^* = M^{2/3} (0.44 m_0) = 0.915 m_0$ with $M=3$. Since the valence band maxima is at the center of the Brillouin zone [15,22,23] $m_{dh}^* = (1.0)m_0$ [8,9,23,34,39].